IEEE Access
Multidisciplinary | Rapid Review | Open Access Journal

Received January 7, 2021, accepted January 17, 2021, date of publication January 20, 2021, date of current version January 28, 2021.

Digital Object Identifier 10.1109/ACCESS.2021.3053060

On the Coupling of Power-Related and Inner Inverter Control Loops of Grid-Forming Converter Systems

MARC DOKUS, (Student Member, IEEE), AND AXEL MERTENS, (Senior Member, IEEE)
Institute for Drive Systems and Power Electronics, Leibniz University Hannover, 30167 Hannover, Germany

Corresponding author: Marc Dokus (marc.dokus@ial.uni-hannover.de)

This work was supported by the Deutsche Forschungsgemeinschaft (DFG, German Research Foundation) under Grant 359921210. The publication of this article was funded by the Open Access Fund of the Leibniz Universität Hannover.

ABSTRACT In the last decade, different control concepts for the synchronisation of voltage-controlled power converters have been proposed in order to form converter-based power systems. The interoperability of these grid-forming power controls is often analysed based on reduced-order models covering only the slow controls or modes. In this article, the coupling of the outer, power-related and inner, inverter output-related control of multiple grid-forming power converter systems is analysed, based on a minimal working example. The elementary study cases each consist of a different grid-forming converter coupled with an external (and passive) grid. Here, the investigated stability problems are already manifested in the simplest possible setup. The analysis of these coupling effects is performed by modelling the system in impedance-based, state-space and phase portrait-based frameworks. In particular, small coupling impedances, like short transmission lines or small short circuit impedances, can be challenging for the controller stability of grid-forming converters while the inner controls can even enhance this issue. The impact of this phenomenon and the participating subsystems are identified in this work. Thus, recommendations concerning modelling techniques and their legitimate assumptions are given. Laboratory experiments validate the performed analysis by indicating a close correlation between analytical models and experimental results.

INDEX TERMS Coupling effects, grid-forming power converter, power-related control, stability analysis, voltage control.

I. INTRODUCTION

Power electronic-based (PE) converters play a key role in future electrical grids. The increasing penetration of renewable distributed energy resources (DER), high-voltage direct current (HVDC) transmission systems and battery energy storage systems (BESS) are, among others, popular examples of the concentration of converters that occurs in the power system sector. In order to properly integrate such a high share of power converters, different control concepts are proposed in the literature [1]. The main concepts can be divided in grid-feeding, grid-supporting and grid-forming controls. In this article, we define these concepts as follows: grid-feeding converters are internally operated as a current source that synchronises to an existing grid voltage; grid-supporting controls include additional functionalities in order to assist in frequency and/or voltage control; grid-forming converters are operated as a voltage source that is often accompanied by an outer power control loop in order to enable parallel operation of multiple entities. The outer (power) control loop is denoted as the power-related control in this article. The concentration of power converters can lead to weak grid scenarios, also referred to as high coupling impedances, that can challenge the interoperability of classical grid-feeding converter clusters [2], [3]. Therefore, the integration of grid-forming controls, which are more robust in weak grid conditions due to their voltage source-like operation [4], [5], is inevitable. In addition, realistic case studies of the Irish power system illustrate the need of grid-forming converters in future grids with 100% DER penetration [6]. However, these systems are more prone to an instability in stiff grid scenarios, also referred to as low coupling impedances. Regardless of the used control algorithms, coupling of neighbouring converter controls through the network impedance is unavoidable and can lead to controller instabilities if not properly designed. The typical destabilising effects are mostly either predominantly caused by the fast inner control loop, filter and grid resonances or by the power-related control loop which

The associate editor coordinating the review of this manuscript and approving it for publication was Zhixiang Zou.

This work is licensed under a Creative Commons Attribution 4.0 License. For more information, see https://creativecommons.org/licenses/by/4.0/

allows to separate the phenomena based on the manifested frequency range. In the former case, these effects are mostly reflected in the medium frequency range between the fundamental and the switching frequency; the latter case is located near the fundamental frequency. In addition, this controller instability is often referred to as harmonic stability regardless of the actual frequency [2].

In the particular case of power-related control (or synchronisation-related) stability, large converter clusters or groups of synchronous generators can interact with each other over wide distances. Models for these fairly large systems are normally based on the assumption of fast electrical transients and inner controls, that are usually at least ten times faster than the outer loop. Thereby, the inner control and grid states are often simplified [7] or even idealised/discarded [8] due to the assumption of negligible impacts on the power-related states [9], [10]. In addition, coherency-based aggregation techniques are used to reduce the model to the relevant participating modes [11], [12]. Thus, the model of large-scale power systems is conventionally reduced either by aggregation of clusters and/or assuming negligible interactions between the inner and outer control loop in the power-related frequency range. These simplifications are sufficient for most of the classical synchronous generator-based power systems due to their strong natural time scale separation. In a power converter setup, both assumptions are no longer valid for some cases [13], [14] and the impact of the latter aspect on the stability will be comprehensively analysed for a basic multi-master microgrid setup in this article.

Different concepts have been used by the power system and power converter community to analyse controller stability aspects, namely: (a) Lyapunov functions [15], [16]; (b) phase portraits [17]; (c) state-space eigenvalue analysis [18], [19] and (d) impedance-based analysis [20], [21]. The methods (a) and (b) can be directly applied to non-linear equations enabling the investigation of large-signal events. Unfortunately, the derivation of Lyapunov functions is often not intuitive and requires model order reductions in order to keep the model manageable. In addition, this analysis is not providing much physical insights. The classical phase-portrait analysis is also based on reduced-order models. In contrast, the techniques (c) and (d) can be applied to complex systems including cascaded control concepts, pulse width modulation (PWM) and sampling delays as well as aliasing effects. In particular, the impedance-based framework is also suitable to analyse large power networks based on the equivalent models due to its modular nature. An exemplary analysis based on sequence impedance models is illustrated in [22] and [23]. However, all these small-signal methods require model linearisation either in time domain or in frequency domain around the steady-state operation point. Hence, a comprehensive analysis can be based on the techniques (b) to (d) in order to cover all relevant aspects while also providing different insights by each framework.

The limits of separating the fast and slow states of grid converters coupled with the power system has only been investigated by a few publications. A comprehensive analysis of the dynamic interactions of grid-feeding converters is elaborated in [24]. Modelling of large-signal events that can jeopardise the synchronisation-related stability of grid-feeding concepts can be based on reduced-order models that neglects grid and inner control states [25], [26]. Nevertheless, the synchronisation process of coupled voltage-controlled entities yields different characteristics that can not be treated in the same manner. In [27], the fast grid states are introduced by a dynamic phasor model (DPM) to accurately cover the impact of large droop gains in grid-forming converters. However, interactions with the inner controls are neglected. The limitations of existing general converter models are explored in [28]. In addition, a more precise model that includes the grid states and some low-frequency characteristics of the inner controls is derived by a systematic model-order reduction method. Since this contribution focuses on legitimate model-order reductions, a comprehensive and general analysis of mutual power-related couplings in grid-forming converters is missing. In [14], a general procedure to truncate the fast states and add a pole-zero representation afterwards (''peel-off and add back'') is used in order to cover a weak grid scenario accurately by considering the impact of the inner control of a grid-forming converter to the overall inductance seen by the connected grid-feeding converter. However, the phenomena that occur in voltage-controlled systems and their interoperability are beyond the scope of that work. A general overview regarding a variety of different synchronisation-related stability aspects is provided in [4].

As a contribution of this article, the authors' aim is to extensively elaborate the constraints of separating the power-related control loop from the fast inner control for two different grid-forming converters that can consist of three different inner control variations. In particular, this analysis will contribute to the identification of the relevant electrical and control states to cover the main phenomena in converter-dominated power-related stability studies that predominantly are based on grid-forming concepts, i.e. microgrids. In addition, even though different objectives are considered in [14] and [28], the presented procedure can be one solution to represent the identified states in a generalised manner.

This article is organised as follows. The considered study case, i.e. the different grid-forming converter controls and their inner control variations, are described in Section II. Subsequently, the equivalent models are derived for the impedance-based, state-space and phase portrait-based framework in Section III. In Section IV, an analysis of the potential oscillatory modes is obtained in each framework. The experimental validation of the performed analysis is described in Section V. Finally, Section VI concludes the article.

II. SYSTEM DESCRIPTION

The key aspects of interactions between the inner and outer control loops of a grid-forming converter system are exemplarily elaborated based on the system in Fig. 1.

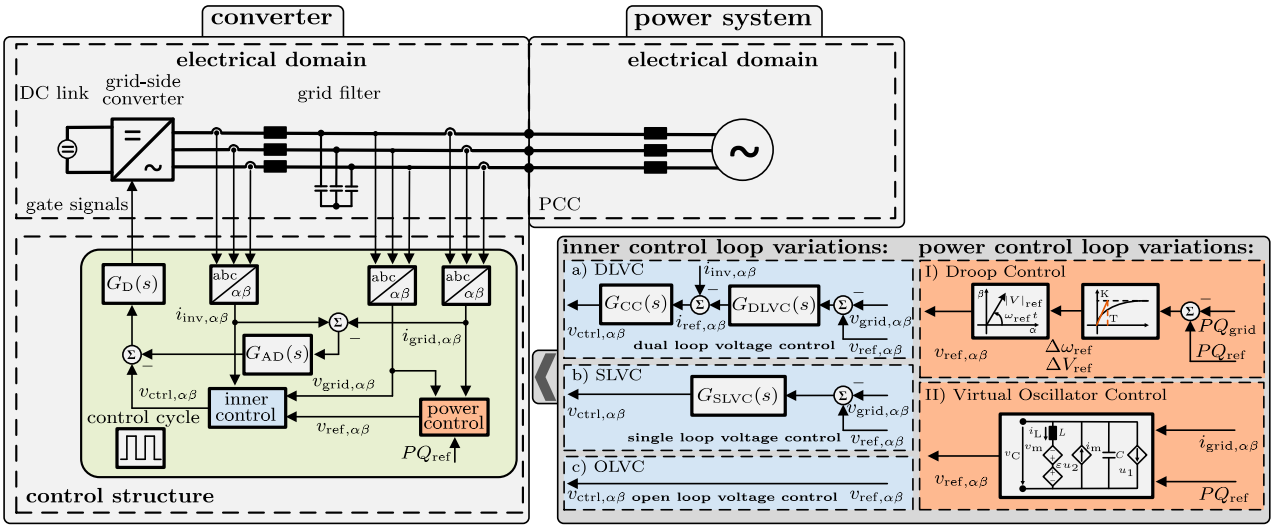

FIGURE 1. System under consideration: grid-forming converter with different variations of the inner inverter output and power-related control loop; inner control: (a) dual loop voltage control, (b) single loop voltage control, (c) open loop voltage control; outer control: (I) droop control, (II) virtual oscillator control; one of the inner (blue) and outer (orange) control blocks can be used in the main control structure to create one of the six investigated cases.

This setup comprises a three-phase (3ph) two-level voltage source converter (VSC) which serves as a widely used example for a DER. The DC link of these systems effectively decouples the grid-side converter from the primary energy side which enables the possibility to represent the power source by an ideal constant voltage source. In addition, some type of battery energy storage is often required for grid-forming converters which emphasises the aforementioned assumptions. An LC filter is used to minimise the harmonic content according to the applicable standards. The voltage at the point of common coupling (PCC) is controlled by the inner inverter output control which receives its reference values from the outer power-related control in a cascaded control framework. In this analysis, three different inner and two different outer control loops can be combined in order to quantify their tendency to interact with each other. The final control setups can be retraced in Fig. 1 by combining one inner control (blue) and one outer control (orange) with the main control structure. In particular, controller ''Ia'' corresponds to the droop-controlled converter with an inner dual loop voltage control.

The complex nature of real power systems that includes the existence of various different loads and DER located across the complete multi-level voltage range are subject to some degree of uncertainty that can rarely be analysed deterministically and thus are omitted. In order to be able to analyse the described coupling effects, a minimal working example (MWE) based on a reduced-order Thévenin equivalent model of a stiff electrical grid is applied. In this work, a weak or stiff grid is always related to the connected converter system rating.

A. POWER-RELATED CONTROL

Two different power-related control algorithms are considered in the analysis process and are explained in the next sections. These outer control loops provide the voltage reference for the inner control in Fig. 1.

1) DROOP CONTROL

The droop control in Fig. 1-I) is defined by the classical P-ω and Q-V linear function, e.g. in [29] and [30], derived for quasi-stationary phasors and described in Laplace domain[1] as

$$\omega_{\mathrm{ref}}(s) = \frac{m_\omega}{P_\mathrm{N}} G_{\mathrm{LP}}(s)(P(s) - P_{\mathrm{ref}}(s)) + \omega_\mathrm{N}, \quad (1)$$

$$\hat{V}_{\mathrm{ref}}(s) = \frac{m_\mathrm{V}}{P_\mathrm{N}} G_{\mathrm{LP}}(s)(Q(s) - Q_{\mathrm{ref}}(s)) + \hat{V}_\mathrm{N},$$

$$\text{with } G_{\mathrm{LP}}(s) = \frac{\omega_{\mathrm{LP}}}{s + \omega_{\mathrm{LP}}}, \quad (2)$$

where m_ω is the frequency droop coefficient; m_V is the voltage droop coefficient; ω_{LP} is the bandwidth of the power filtering; ω_N is the nominal frequency; $\hat{V}_\mathrm{N}$ is the nominal voltage amplitude[2]; P_N is the rated power; $P_{\mathrm{ref}}(s)/Q_{\mathrm{ref}}(s)$ are the reference values for active and reactive power; $P(s)/Q(s)$ are the instantaneous active and reactive power; $s = j\omega$ is the complex frequency.

The instantaneous power values are calculated in time domain based on the measured and unfiltered grid currents $i_{\mathrm{grid},\alpha\beta}(t)$ and grid voltages $v_{\mathrm{grid},\alpha\beta}(t)$ transformed to the $\alpha\beta$-frame

$$p(t) = \frac{3}{2}\left(v_{\mathrm{grid},\alpha}(t) i_{\mathrm{grid},\alpha}(t) + v_{\mathrm{grid},\beta}(t) i_{\mathrm{grid},\beta}(t)\right), \quad (3)$$

$$q(t) = \frac{3}{2}\left(v_{\mathrm{grid},\beta}(t) i_{\mathrm{grid},\alpha}(t) - v_{\mathrm{grid},\alpha}(t) i_{\mathrm{grid},\beta}(t)\right). \quad (4)$$

[1]The Laplace operator is denoted as $s = j\omega$.

[2]The amplitude of sinusoidal signals are represented by the hat operator, i.e. $\hat{x}$.

The voltage reference can be represented as a space vector[3] in $\alpha\beta$-frame by combining (1) and (2) which yields

$$\underline{V}_{\mathbf{ref},\boldsymbol{\alpha\beta}}(t) = \hat{V}_{\mathrm{ref}} e^{j\omega_{\mathrm{ref}} t}. \tag{5}$$

The presented control formulation is equivalent to a first-order low-pass filter with a time constant of $T = \frac{1}{\omega_{\mathrm{LP}}}$ and proportional gain of $K = \left\{\frac{m_\omega}{P_{\mathrm{N}}}, \frac{m_{\mathrm{V}}}{P_{\mathrm{N}}}\right\}$ as illustrated in Fig. 1; or alternatively, it is equivalent to a synchronous generator with a droop coefficient of $\left\{D_{\mathrm{p}} = \frac{P_{\mathrm{N}}}{m_\omega \omega_{\mathrm{N}}}, D_{\mathrm{q}} = \frac{P_{\mathrm{N}}}{m_{\mathrm{V}}}\right\}$ and a virtual inertia of $\left\{J_{\mathrm{p}} = \frac{D_{\mathrm{p}}}{\omega_{\mathrm{LP}}}, J_{\mathrm{q}} = \frac{D_{\mathrm{q}}}{\omega_{\mathrm{LP}}}\right\}$ as explained in [31]. Here, the applied droop parameters in Table 2 of the appendix are chosen according to the nominal grid operation ($\Delta f_{\max} = 0.5\,\mathrm{Hz}$ and $\Delta|V|_{\max} = 5\,\%$). However, a design procedure based on simplified transfer functions can be more suitable in order to obtain the desired dynamic performance [32].

2) VIRTUAL OSCILLATOR CONTROL (VOC)

The promising virtual oscillator control concept in Fig. 1-II) that is intrinsically compatible with 3ph power systems has been chosen from a variety of different non-linear oscillator algorithms to be compared with the classical droop control. The basic concept and its design is analysed in [33]. This power-related control can be formulated in time domain by

$$\begin{aligned}\dot{v}_{\mathrm{ref},\alpha}(t) = {} & \frac{\zeta}{k_{\mathrm{v}}^2}(2V_{\mathrm{N}}^2 - |v_{\mathrm{ref},\alpha\beta}(t)|^2)v_{\mathrm{ref},\alpha}(t) - \omega_{\mathrm{N}} v_{\mathrm{ref},\beta}(t) \\ & - \frac{k_{\mathrm{v}} k_{\mathrm{i}}}{C}\big(\cos\varphi(i_{\mathrm{grid},\alpha}(t) - i_{\mathrm{ref},\alpha}(t)) \\ & \quad - \sin\varphi(i_{\mathrm{grid},\beta}(t) - i_{\mathrm{ref},\beta}(t))\big), \end{aligned} \tag{6}$$

$$\begin{aligned}\dot{v}_{\mathrm{ref},\beta}(t) = {} & \frac{\zeta}{k_{\mathrm{v}}^2}(2V_{\mathrm{N}}^2 - |v_{\mathrm{ref},\alpha\beta}(t)|^2)v_{\mathrm{ref},\beta}(t) + \omega_{\mathrm{N}} v_{\mathrm{ref},\alpha}(t) \\ & - \frac{k_{\mathrm{v}} k_{\mathrm{i}}}{C}\big(\sin\varphi(i_{\mathrm{grid},\alpha}(t) - i_{\mathrm{ref},\alpha}(t)) \\ & \quad + \cos\varphi(i_{\mathrm{grid},\beta}(t) - i_{\mathrm{ref},\beta}(t))\big), \end{aligned} \tag{7}$$

where C is a virtual capacitance; $\omega_{\mathrm{N}} = \frac{1}{\sqrt{LC}}$ is the natural oscillator frequency; L is a virtual inductance; V_{N} is the nominal voltage; ζ is the convergence speed constant; $k_{\mathrm{v}}/k_{\mathrm{i}}$ are scaling factors for the voltages and currents, respectively; φ can be used to consider the effect of the voltage amplitude and frequency on the active and reactive power flow for any resistive-inductive power system, i.e. $\varphi = \frac{\pi}{2}$ equals the standard droop control; $i_{\mathrm{grid},\alpha\beta}(t)$ are the measured grid currents.

The reference currents $i_{\mathrm{ref},\alpha\beta}(t)$ are calculated based on the internal voltage reference $v_{\mathrm{ref},\alpha\beta}(t)$ and a setpoint signal for the active and reactive power $P_{\mathrm{ref}}(t)/Q_{\mathrm{ref}}(t)$ which are defined as

$$i_{\mathrm{ref},\alpha}(t) = \frac{2}{3|v_{\mathrm{ref},\alpha\beta}(t)|}\big(v_{\mathrm{ref},\alpha}(t)P_{\mathrm{ref}}(t) + v_{\mathrm{ref},\beta}(t)Q_{\mathrm{ref}}(t)\big), \tag{8}$$

$$i_{\mathrm{ref},\beta}(t) = \frac{2}{3|v_{\mathrm{ref},\alpha\beta}(t)|}\big(v_{\mathrm{ref},\beta}(t)P_{\mathrm{ref}}(t) - v_{\mathrm{ref},\alpha}(t)Q_{\mathrm{ref}}(t)\big). \tag{9}$$

[3]Space vectors are written in bold letters with an underscore.

The voltage reference can be represented as a space vector in $\alpha\beta$-frame by combining (6) and (7) which yields

$$\underline{V}_{\mathbf{ref},\boldsymbol{\alpha\beta}}(t) = v_{\mathrm{ref},\alpha}(t) + j v_{\mathrm{ref},\beta}(t). \tag{10}$$

Similar steady-state characteristics as for the droop control can be achieved by choosing $C = \frac{1}{\sqrt{2}(1-m_{\mathrm{V}}/\hat{V}_{\mathrm{N}})^2 m_\omega}$ and $\zeta = \frac{\sqrt{2}}{4(1-m_{\mathrm{V}}/\hat{V}_{\mathrm{N}})^2 C} \cdot \frac{1}{1-(1-m_{\mathrm{V}}/\hat{V}_{\mathrm{N}})^2}$ in the design process.[4] The steady state voltage phasor of the virtual oscillator is defined as follows:

$$\hat{V}_{\mathrm{ref}} = \hat{V}_{\mathrm{N}}\left(1 + \sqrt{1 + \frac{2k_{\mathrm{v}}k_{\mathrm{i}}}{3C\zeta V_{\mathrm{N}}}\big(Q_{\mathrm{ref}} - Q_0\big)}\right)^{\frac{1}{2}}, \tag{11}$$

$$\omega_{\mathrm{ref}} = \frac{2k_{\mathrm{v}}k_{\mathrm{i}}}{3C\hat{V}_{\mathrm{ref}}^2}\big(P_{\mathrm{ref}} - P_0\big) + \omega_{\mathrm{N}}. \tag{12}$$

Here, the steady-state active and reactive power is denoted as P_0/Q_0.

In general, a virtual oscillator stabilises arbitrary waveforms to a sinusoidal steady state output (voltage) that is synchronised to the input (current) without assuming well-defined phasors, which yields a superior control bandwidth for the nominal grid operation region [34], [35]. However, this concept can be more prone to oscillations. In addition, (6) - (10) is equivalent to the electrical tank circuit illustrated in Fig. 1-II) with

$$\begin{aligned} u_1(t) = {} & k_{\mathrm{i}}\big(\cos\varphi(i_{\mathrm{grid},\alpha}(t) - i_{\mathrm{ref},\alpha}(t)) \\ & \quad - \sin\varphi(i_{\mathrm{grid},\beta}(t) - i_{\mathrm{ref},\beta}(t))\big), \end{aligned} \tag{13}$$

$$\begin{aligned} u_2(t) = {} & k_{\mathrm{i}}\big(\sin\varphi(i_{\mathrm{grid},\alpha}(t) - i_{\mathrm{ref},\alpha}(t)) \\ & \quad + \cos\varphi(i_{\mathrm{grid},\beta}(t) - i_{\mathrm{ref},\beta}(t))\big), \end{aligned} \tag{14}$$

$$i_{\mathrm{m}}(t) = \frac{\zeta}{\varepsilon\omega_{\mathrm{N}}k_{\mathrm{v}}^2}(2V_{\mathrm{N}}^2 - |v_{\mathrm{ref},\alpha\beta}(t)|^2)v_{\mathrm{C}}(t), \tag{15}$$

$$v_{\mathrm{m}}(t) = \frac{\zeta}{\omega_{\mathrm{N}}k_{\mathrm{v}}^2}(2V_{\mathrm{N}}^2 - |v_{\mathrm{ref},\alpha\beta}(t)|^2)\varepsilon i_{\mathrm{L}}(t), \tag{16}$$

and the reference voltage $v_{\mathrm{ref},\alpha\beta}(t) = k_{\mathrm{v}}(v_{\mathrm{C}}(t) + j\varepsilon i_{\mathrm{L}}(t))$; $\varepsilon = \sqrt{\frac{L}{C}}$ is a scaling factor [33]. Here, the droop and VOC concept are designed according to the aforementioned rules and the parameters are listed in Table 2.

B. INNER INVERTER OUTPUT CONTROL

Three different inner control algorithms are considered in the analysis process of the setup in Fig. 1 and are explained in the next sections.

1) DUAL LOOP VOLTAGE CONTROL (DLVC)

In case of Fig. 1-a), the inner control includes two discrete proportional and resonant controllers, an active damping scheme and the inherent pulse width modulation (PWM) and sampling delay expressed in Laplace domain as $G_{\mathrm{CC}}(s)$, $G_{\mathrm{DLVC}}(s)$, $G_{\mathrm{AD}}(s)$ and $G_{\mathrm{D}}(s)$, respectively. The capacitor current is used as a feedback for the active damping procedure

[4]In this case, the system is scaled based on $k_{\mathrm{v}} = V_{\mathrm{N}}$ and $k_{\mathrm{i}} = 3\frac{V_{\mathrm{N}}}{P_{\mathrm{N}}}$.

according to [36]. The equivalent continuous time transfer functions (TF) are defined as

$$G_{\mathrm{CC}}(s) = k_{\mathrm{P,I}}\left(1+\frac{1}{T_{\mathrm{i,I}}}\frac{2\omega_{\mathrm{BW,I}}(s\cos\phi_{\mathrm{I}}-\omega_0\sin\phi_{\mathrm{I}})}{s^2+2\omega_{\mathrm{BW,I}}s+\omega_0^2}\right), \quad (17)$$

$$G_{\mathrm{DLVC}}(s) = k_{\mathrm{P,V,DL}}\left(1 + \frac{1}{T_{\mathrm{i,V,DL}}}\frac{2\omega_{\mathrm{BW,V}}(s\cos\phi_{\mathrm{V}}-\omega_0\sin\phi_{\mathrm{V}})}{s^2+2\omega_{\mathrm{BW,V}}s+\omega_0^2}\right), \quad (18)$$

$$G_{\mathrm{AD}}(s) = \frac{K_{\mathrm{rc}}s}{s+\omega_{\mathrm{rc}}}, G_{\mathrm{D}}(s) = \frac{e^{-sT_{\mathrm{s}}}-e^{-s2T_{\mathrm{s}}}}{sT_{\mathrm{s}}}. \quad (19)$$

The current and voltage control are specified by a proportional and integral gain $k_{\mathrm{P}}/T_{\mathrm{i}}$, a bandwidth ω_{BW} for the resonator and a phase lead ϕ; K_{rc} and ω_{rc} denote the proportional gain and bandwidth of the active damping scheme; the sampling period is defined as T_{s}.

2) SINGLE LOOP VOLTAGE CONTROL (SLVC)

The single loop voltage control in Fig. 1-b) consists of one discrete proportional + resonant controller $G_{\mathrm{SLVC}}(s)$ and the identical active damping concept $G_{\mathrm{AD}}(s)$, inherent PWM and sampling delay $G_{\mathrm{D}}(s)$. The single controller maintains the voltage at the PCC and is defined by the continuous time transfer function

$$G_{\mathrm{SLVC}}(s) = k_{\mathrm{P,V,SL}}\left(1 + \frac{1}{T_{\mathrm{i,V,SL}}}\frac{2\omega_{\mathrm{BW,V}}(s\cos\phi_{\mathrm{V}}-\omega_0\sin\phi_{\mathrm{V}})}{s^2+2\omega_{\mathrm{BW,V}}s+\omega_0^2}\right). \quad (20)$$

A design procedure for this type of control method can be found in [37]. In general, it is expected that the LC filter resonance frequency and possibly other resonances are less damped due to the missing inner current control loop which provides additional damping.

3) OPEN LOOP VOLTAGE CONTROL (OLVC)

In case of the open loop control concept in Fig. 1-c), the reference voltage of the power-related control is directly utilised to generate the PWM signals. Thus, only the equivalent delay $G_{\mathrm{D}}(s)$ and an identical active damping scheme $G_{\mathrm{AD}}(s)$ are included in this control approach. The damping concept may be necessary to suppress high frequency interactions while a similar damping performance as for the SLVC case is expected.

C. ELECTRICAL POWER SYSTEM

The MWE in Fig. 1 is identified to be suitable to cover possible coupling effects of the inner and outer control loops of grid-forming converters manifested as sideband oscillations [4], [38]. In that respect, the system is condensed to connecting an inductive and stiff Thévenin equivalent with a converter based on the aforementioned control concepts. Thus, the electrical power system is represented as a passive element consisting of an ideal voltage source (here: ideal voltage-controlled entity) with a relative small and mostly inductive impedance $Z_{\mathrm{grid}} = R_{\mathrm{grid}} + j\omega L_{\mathrm{grid}}$. In this work, a small or large impedance is always referred to the converter impedance in Section III-A.

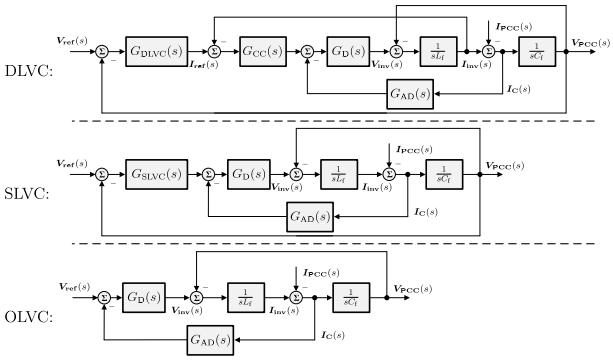

FIGURE 2. Block diagram of the three considered inner inverter output control concepts in frequency domain: DLVC, SLVC and OLVC.

III. SYSTEM MODELLING

Different concepts and modelling frameworks have been developed and adapted over the last decades to analyse power systems considering their special properties. Each concept offers its own advantages and disadvantages in the analysis procedure, e.g. degree of modelling assumptions or ability to cover non-linear effects. In order to overcome individual drawbacks and rather emphasise each benefit, the described system is investigated in an impedance-based framework, in state space and based on phase portraits to guarantee a comprehensive analysis procedure.

In particular, the detailed small-signal impedance model is used to identify oscillatory modes of the terminal currents and voltages, while the coupling path of inner and outer control loop is investigated based on the state-space eigenvalues. Transient responses to large-signal disturbances are covered by phase portrait models.

A. EQUIVALENT IMPEDANCE MODEL

The fundamental concept of representing each subsystem of a power network in frequency domain by an impedance with an ideal voltage source (Thévenin equivalent) or an admittance with an ideal current source (Norton equivalent) can be utilised to analyse the local stability of two subsystems, e.g. the device under test and the electrical grid.

The mathematical equations of each converter system can be reformulated to meet these input-output characteristics yielding detailed high-order models that can cover discrete controllers, aliasing effects and includes an accurate PWM and sampling representation. In addition, the modularity of these models, i.e. the fact that characteristics of each subsystem can be often calculated separately, allows to easily apply this framework for a large-scale power system analysis.

In contrast, only linear input-output characteristics can be covered in the local stability analysis of two subsystems and

identifying the contribution of each component, i.e. converter in the grid, to a specific oscillatory mode can only be done with additional effort and is somewhat limited [19]. In general, this framework is restricted to the small-signal stability analysis of different operation points.

1) INNER INVERTER OUTPUT CONTROL

The three different inner inverter controls in Fig. 1 are rearranged and illustrated as a block diagram in Fig. 2 in order to obtain the equivalent impedance and control characteristics.

a: DUAL LOOP VOLTAGE CONTROL (DLVC)

The basic model of a dual loop voltage-controlled converter can be derived based on Fig. 2 and is published in [21]. The input-output characteristics are described by (21) where C_f and L_f are the filter capacitance and inductance; resistances are omitted for the sake of brevity. Here, the actually implemented discrete controller TFs and the aliasing aspects in [39] are considered in order to achieve a good model fidelity for frequencies up to the sampling frequency f_s.

Hereby, the Thévenin equivalent of a dual loop voltage-controlled converter is defined by $\{G_{\mathrm{cl,DLVC}}(s), Z_{\mathrm{C,DLVC}}(s)\}$ in (21). The frequency response of the closed loop inner control $G_{\mathrm{cl,DLVC}}(s)$ is shown in Fig. 3.

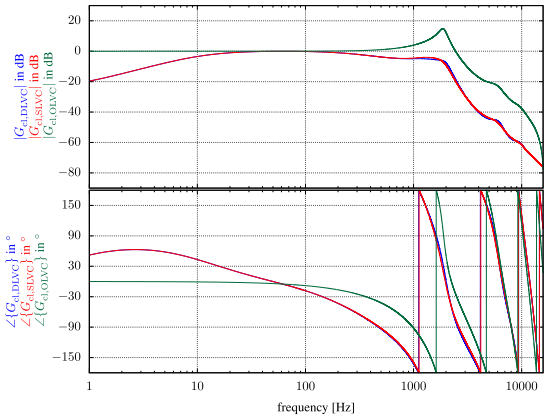

FIGURE 3. Bode plots of the three considered inner inverter output control concepts, whose parameters are listed in Table 2: DLVC, SLVC and OLVC.

b: SINGLE LOOP VOLTAGE CONTROL (SLVC)

Consequently, a model of a single loop voltage-controlled converter is derived based on Fig. 2 which yields the equivalent TFs in (22). Again, all resistances are neglected.

The converter system is completely modelled by the developed Thévenin equivalent $\{G_{\mathrm{cl,SLVC}}(s), Z_{\mathrm{C,SLVC}}(s)\}$ in (22). In addition, the closed loop control characteristics $G_{\mathrm{cl,SLVC}}(s)$ are illustrated in Fig. 3.

c: OPEN LOOP VOLTAGE CONTROL (OLVC)

A similar representation is achieved for an open loop voltage-controlled converter in Fig. 2. Reformulating the filter equations in order to quantify the impact of the inverter voltage and PCC current on the terminal voltage yields (23) for the non-resistive case.

The Thévenin equivalent is described based on the closed loop control TF and the converter impedance $\{G_{\mathrm{cl,OLVC}}(s), Z_{\mathrm{C,OLVC}}(s)\}$ in (23). The control TF is also shown in Fig. 3.

2) LINEARISED POWER-RELATED CONTROL

A small-signal model of the considered variations of a grid-forming converter can be derived by linking the input/output in (1) - (5) or in (6) - (10) with the inner inverter output control in (21) - (23) and conduct the necessary linearisation.

a: DROOP CONTROL

The model of a droop-controlled converter is published in [40] and can be derived by specifying an operation point based on the steady-state values $\boldsymbol{v}_\mathbf{PCC} = \hat{V}_0 e^{j\varphi_\mathrm{u}}, \boldsymbol{i}_\mathbf{PCC} = \hat{i}_0 e^{j\varphi_\mathrm{i}}$ and $\omega = \omega_0$ at the PCC (eq. to subscsript 'grid' in Fig. 1). A small-signal current $\boldsymbol{di}(\widetilde{s})$ and voltage $\boldsymbol{dV}(\widetilde{s})$ perturbation with the disturbance frequency $\widetilde{s} = j\omega_\mathrm{d}$ are introduced which

$$DLVC\begin{cases} G_{\mathrm{cl,DLVC}}(s) = \left.\dfrac{\boldsymbol{V}_\mathbf{PCC}(s)}{\boldsymbol{V}_\mathbf{ref}(s)}\right|_{\boldsymbol{I}_\mathbf{PCC}(s)=0} = \dfrac{G_{\mathrm{CC}}(s)G_{\mathrm{DLVC}}(s)G_\mathrm{D}(s)}{C_\mathrm{f}L_\mathrm{f}s^2 + C_\mathrm{f}G_{\mathrm{AD}}(s)G_\mathrm{D}(s)s + C_\mathrm{f}G_{\mathrm{CC}}(s)G_\mathrm{D}(s)s + G_{\mathrm{CC}}(s)G_{\mathrm{DLVC}}(s)G_\mathrm{D}(s) + 1} \\ Z_{\mathrm{C,DLVC}}(s) = \left.\dfrac{\boldsymbol{V}_\mathbf{PCC}(s)}{\boldsymbol{I}_\mathbf{PCC}(s)}\right|_{\boldsymbol{V}_\mathbf{ref}(s)=0} = \dfrac{L_\mathrm{f}s + G_{\mathrm{CC}}(s)G_\mathrm{D}(s)}{C_\mathrm{f}L_\mathrm{f}s^2 + C_\mathrm{f}G_{\mathrm{AD}}(s)G_\mathrm{D}(s)s + C_\mathrm{f}G_{\mathrm{CC}}(s)G_\mathrm{D}(s)s + G_{\mathrm{CC}}(s)G_{\mathrm{DLVC}}(s)G_\mathrm{D}(s) + 1} \end{cases} \tag{21}$$

$$SLVC\begin{cases} G_{\mathrm{cl,SLVC}}(s) = \left.\dfrac{\boldsymbol{V}_\mathbf{PCC}(s)}{\boldsymbol{V}_\mathbf{ref}(s)}\right|_{\boldsymbol{I}_\mathbf{PCC}(s)=0} = \dfrac{G_{\mathrm{SLVC}}(s)G_\mathrm{D}(s)}{C_\mathrm{f}L_\mathrm{f}s^2 + C_\mathrm{f}G_{\mathrm{AD}}(s)G_\mathrm{D}(s)s + G_{\mathrm{SLVC}}(s)G_\mathrm{D}(s) + 1} \\ Z_{\mathrm{C,SLVC}}(s) = \left.\dfrac{\boldsymbol{V}_\mathbf{PCC}(s)}{\boldsymbol{I}_\mathbf{PCC}(s)}\right|_{\boldsymbol{V}_\mathbf{ref}(s)=0} = \dfrac{L_\mathrm{f}s}{C_\mathrm{f}L_\mathrm{f}s^2 + C_\mathrm{f}G_{\mathrm{AD}}(s)G_\mathrm{D}(s)s + G_{\mathrm{SLVC}}(s)G_\mathrm{D}(s) + 1} \end{cases} \tag{22}$$

$$OLVC\begin{cases} G_{\mathrm{cl,OLVC}}(s) = \left.\dfrac{\boldsymbol{V}_\mathbf{PCC}(s)}{\boldsymbol{V}_\mathbf{ref}(s)}\right|_{\boldsymbol{I}_\mathbf{PCC}(s)=0} = \dfrac{G_\mathrm{D}(s)}{C_\mathrm{f}L_\mathrm{f}s^2 + C_\mathrm{f}G_{\mathrm{AD}}(s)G_\mathrm{D}(s)s + 1} \\ Z_{\mathrm{C,OLVC}}(s) = \left.\dfrac{\boldsymbol{V}_\mathbf{PCC}(s)}{\boldsymbol{I}_\mathbf{PCC}(s)}\right|_{\boldsymbol{V}_\mathbf{ref}(s)=0} = \dfrac{L_\mathrm{f}s}{C_\mathrm{f}L_\mathrm{f}s^2 + C_\mathrm{f}G_{\mathrm{AD}}(s)G_\mathrm{D}(s)s + 1} \end{cases} \tag{23}$$

yields the following phasors[5]

$$\boldsymbol{V}_{\mathbf{PCC}}(\widetilde{s}) = \big(\hat{V}_0 + \boldsymbol{dV}(\widetilde{s})\big), \tag{24}$$

$$\boldsymbol{I}_{\mathbf{PCC}}(\widetilde{s}) = \big(\hat{i}_0 e^{j(\varphi_\mathrm{u}-\varphi_\mathrm{i})} + \boldsymbol{di}(\widetilde{s})\big). \tag{25}$$

Here, the steady state voltage is aligned with the real axis which simplifies the model derivation. Furthermore, the measured active and reactive power required for the droop control in (1) - (5) can be calculated based on the instantaneous power in frequency domain defined as

$$\boldsymbol{S}(\widetilde{s}) = P(\widetilde{s}) + jQ(\widetilde{s}) = \frac{3}{2}\boldsymbol{V}_{\mathbf{PCC}}(\widetilde{s})\overline{\boldsymbol{I}}_{\mathbf{PCC}}(\widetilde{s}), \tag{26}$$

where $\overline{\boldsymbol{I}}_{\mathbf{PCC}}(\widetilde{s})$ denotes the conjugate complex of $\boldsymbol{I}_{\mathbf{PCC}}(\widetilde{s})$. Neglecting any cross coupling between $\boldsymbol{di}(\widetilde{s})$ and $\boldsymbol{dV}(\widetilde{s})$ as part of the linearisation and only addressing the disturbance response yields the following small-signal droop equations

$$\boldsymbol{d\theta}_{\mathbf{ref}}(\widetilde{s}) = \frac{3m_\omega}{2P_\mathrm{N}\widetilde{s}} G_\mathrm{LP}(\widetilde{s})\big(\mathrm{Re}\{\hat{V}_0\overline{\boldsymbol{di}}(\widetilde{s})\} + \mathrm{Re}\{\boldsymbol{dV}(\widetilde{s})\overline{\boldsymbol{i_0}}\}\big), \tag{27}$$

$$\boldsymbol{d}\hat{\boldsymbol{V}}_{\mathrm{ref}}(\widetilde{s}) = \frac{3m_\mathrm{V}}{2P_\mathrm{N}} G_\mathrm{LP}(\widetilde{s})\big(\mathrm{Im}\{\hat{V}_0\overline{\boldsymbol{di}}(\widetilde{s})\} + \mathrm{Im}\{\boldsymbol{dV}(\widetilde{s})\overline{\boldsymbol{i_0}}\}\big), \tag{28}$$

in which $\boldsymbol{i_0} = \hat{i}_0 e^{j(\varphi_\mathrm{u}-\varphi_\mathrm{i})}$ is used for the sake of brevity.

These equations describe the input-output characteristic of the droop control to current and voltage disturbances which are propagated to the inner control loop. The coupling of both control loops is established by dictating a reference value for the PCC voltage expressed as

$$\boldsymbol{V}_{\mathbf{ref}}(s) = \big(\hat{V}_0 + \boldsymbol{d}\hat{\boldsymbol{V}}_{\mathrm{ref}}(\widetilde{s})\big)e^{j(\boldsymbol{d\theta}_{\mathbf{ref}}(\widetilde{s})+\omega_0 t)}, \tag{29}$$

where the frequency (or Laplace operator) $s = j\omega$ in $\alpha\beta$-frame is the sum of a disturbance frequency $\widetilde{s} = j\omega_\mathrm{d}$ and the steady-state frequency $j\omega = j\omega_0$. The Thévenin equivalent of the inner controls in (21) - (23) can be linked with the outer control by describing the PCC voltage as

$$\boldsymbol{V}_{\mathbf{PCC}}(s) = G_\mathrm{cl}(s)\boldsymbol{V}_{\mathbf{ref}}(s) - Z_\mathrm{C}(s)\boldsymbol{I}_{\mathbf{PCC}}(s). \tag{30}$$

In order to combine (29) with (30) and effectively derive a linear model, (29) needs to be simplified using the relation $e^{j(\boldsymbol{d\theta}_{\mathbf{ref}}(s)+\omega_0 t)} \approx \big(1 + j\boldsymbol{d\theta}_{\mathbf{ref}}(s)\big)e^{j\omega_0 t}$. In addition, cross coupling between $\boldsymbol{d}\hat{\boldsymbol{V}}_{\mathrm{ref}}(\widetilde{s})$ and $\boldsymbol{d\theta}_{\mathbf{ref}}(\widetilde{s})$ is neglected in this step such that the small-signal behaviour can be introduced as

$$\boldsymbol{dV}_{\mathbf{ref}}(s) = \left(\boldsymbol{d}\hat{\boldsymbol{V}}_{\mathrm{ref}}(\widetilde{s}) + j\boldsymbol{d\theta}_{\mathbf{ref}}(\widetilde{s})\hat{V}_0\right)e^{j\omega_0 t}, \tag{31}$$

$$\begin{aligned}\boldsymbol{dV}_{\mathbf{ref}}(s) = \frac{3}{2P_\mathrm{N}} G_\mathrm{LP}(\widetilde{s})\Bigg(&\frac{m_\omega}{\widetilde{s}}\hat{V}_0 j\,\mathrm{Re}\{\hat{V}_0\overline{\boldsymbol{di}}(\widetilde{s}) + \boldsymbol{dV}(\widetilde{s})\overline{\boldsymbol{i_0}}\}\\ &+m_\mathrm{V}\,\mathrm{Im}\{\hat{V}_0\overline{\boldsymbol{di}}(\widetilde{s}) + \boldsymbol{dV}(\widetilde{s})\overline{\boldsymbol{i_0}}\}\Bigg)e^{j\omega_0 t}.\end{aligned} \tag{32}$$

Finally, the converter impedance $Z_\mathrm{C}(s)$ can be elaborated by substituting (32) in (30) and applying the relations $\mathrm{Im}\{X\} = \frac{X-\overline{X}}{2j}$ and $\mathrm{Re}\{X\} = \frac{X+\overline{X}}{2}$ so that the system is described by a linear equation system

$$\mathbf{A}\begin{pmatrix}\square\square\\ \square\square\end{pmatrix}\underline{x} = \underline{B}\begin{pmatrix}\square\\ \square\end{pmatrix}, \tag{33}$$

where $\square$ indicates non-zero matrix/vector[6] entries. These equations yield a 2×2 sequence impedance matrix which is also called a modified sequence-domain model [41]. Details of the equation system can be found in Appendix A.

The primary single-input-single-output (SISO) characteristic $Z_\mathrm{C}(s) = \frac{\boldsymbol{dV}(s)}{\boldsymbol{di}(s)}$ can be extracted by solving this equation system. In particular, the system response, e.g. $Z_\mathrm{C}(s)$, not only differs for positive- and negative-sequence perturbations of $\boldsymbol{di}(s)$ but also introduces a second voltage component $\boldsymbol{dV}(2j\omega_0 - s)$ which is often called a mirrored harmonic.

Any aspects of interactions between $\boldsymbol{dV}(s)$ and $\boldsymbol{dV}(2j\omega_0 - s)$ in coupled power systems can be included in a small-signal analysis following the steps in [42]. In [43], the authors derive a procedure to bypass the necessary (generalised Nyquist [44]) analysis of such multiple-input-multiple-output (MIMO) systems by defining the model differently in order to extract one characteristic SISO transfer function that can be used for a stability analysis.

However, since the power-related frequencies are weakly coupled in this case (small off-diagonal elements in the impedance matrix; evaluated according to [41]), only the primary impedance $Z_\mathrm{C}(s)$ is considered which is sufficient for most stability phenomena.

b: VIRTUAL OSCILLATOR CONTROL (VOC)

The model of a VOC-controlled converter can be derived in a similar fashion, in particular by specifying an operation point based on the steady-state values $\boldsymbol{v}_{\mathbf{PCC}} = \hat{V}_0 e^{j\varphi_\mathrm{u}}$, $\boldsymbol{i}_{\mathbf{PCC}} = \hat{i}_0 e^{j\varphi_\mathrm{i}}$ and $\omega = \omega_0$ while the identical voltage and current perturbations, i.e. (24) and (25), are applied.
In addition, sequence domain-like equivalents of (6) - (10) can be derived in Laplace domain introducing

$$\boldsymbol{I}_{\mathbf{ref}}(s) = i_{\mathrm{ref},\alpha}(s) + ji_{\mathrm{ref},\beta}(s), \tag{34}$$

$$\boldsymbol{V}_{\mathbf{ref}}(s) = v_{\mathrm{ref},\alpha}(s) + jv_{\mathrm{ref},\beta}(s), \tag{35}$$

$$\boldsymbol{I}_{\mathbf{PCC}}(s) = i_{\mathrm{grid},\alpha}(s) + ji_{\mathrm{grid},\beta}(s), \tag{36}$$

$$S_\mathrm{ref} = P_\mathrm{ref} + jQ_\mathrm{ref}. \tag{37}$$

This enables the possibility to derive an input-output characteristic for positive and negative sequences in the $\alpha\beta$-frame.

Thus, the equation system in (6) - (7) can be described by phasors in frequency domain as

$$\begin{aligned}s\boldsymbol{V}_{\mathbf{ref}}(s) = &\left(\frac{2\zeta}{k_\mathrm{v}^2}V_\mathrm{N}^2 - \frac{\zeta}{k_\mathrm{v}^2}|\boldsymbol{V}_{\mathbf{ref}}(s)|^2 + j\omega_\mathrm{N}\right)\boldsymbol{V}_{\mathbf{ref}}(s)\\ &-\frac{k_\mathrm{i}k_\mathrm{v}}{C}\left(\boldsymbol{I}_{\mathbf{PCC}}(s) - \frac{2e^{j\varphi}}{3|\boldsymbol{V}_{\mathbf{ref}}(s)|^2}\overline{S}_\mathrm{ref}\boldsymbol{V}_{\mathbf{ref}}(s)\right).\end{aligned} \tag{38}$$

where $\overline{\boldsymbol{S}}_{\mathbf{ref}}$ denotes the conjugate complex of the reference value for the apparent power $\boldsymbol{S}_{\mathbf{ref}}$.

A linear equivalent impedance can be derived considering small-signal disturbances in $\boldsymbol{V}_{\mathbf{ref}}(s)$ so that the following equations can be obtained

$$\boldsymbol{V}_{\mathbf{ref}}(s) = \hat{V}_0 e^{j\omega_0 t} + \boldsymbol{dV}_{\mathbf{ref}}(\widetilde{s}), \tag{39}$$

[5] Phasors are denoted with bold letters, small-signal perturbations of these phasors are represented by a "d" in front of the letters and steady-state values are expressed by "0" in the subscript.

[6] Matrices are expressed by bold letters and vectors are denoted with an underscore.

$$|\boldsymbol{V}_{\mathbf{ref}}(s)|^2 \approx \hat{V}_0^2 + \hat{V}_0\big(\boldsymbol{dV}_{\mathbf{ref}}(\widetilde{s}) + \overline{\boldsymbol{dV}}_{\mathbf{ref}}(\widetilde{s})\big), \quad (40)$$

where $\overline{\boldsymbol{dV}}_{\mathbf{ref}}(\widetilde{s})$ denotes the conjugate complex of $\boldsymbol{dV}_{\mathbf{ref}}(\widetilde{s})$ equivalent to the mirrored disturbance frequency at $s_\mathrm{m} = 2j\omega_0 - s$ for the droop-controlled system in the $\alpha\beta$-frame.

Furthermore, only accounting for disturbances that occur as a product of a steady-state value and a perturbation, and thus effectively neglecting cross couplings between any small-signal variables, e.g. $\boldsymbol{dV}_{\mathbf{ref}}(\widetilde{s})$ or $\boldsymbol{di}(\widetilde{s})$, yields

$$\widetilde{s}\boldsymbol{dV}_{\mathbf{ref}}(\widetilde{s}) = \left(\frac{2\zeta}{k_\mathrm{v}^2}V_\mathrm{N}^2 + j\omega_\mathrm{N}\right)\boldsymbol{dV}_{\mathbf{ref}}(\widetilde{s}) - \frac{k_\mathrm{i}k_\mathrm{v}}{C}\boldsymbol{di}(\widetilde{s}) + \frac{2k_\mathrm{i}k_\mathrm{v}e^{j\varphi}}{3C\hat{V}_0^2}\overline{\boldsymbol{S}}_{\mathbf{ref}}\boldsymbol{dV}_{\mathbf{ref}}(\widetilde{s}) - \frac{\zeta}{k_\mathrm{v}^2}\,\Gamma\{|\boldsymbol{V}_{\mathbf{ref}}(s)|^2\boldsymbol{V}_{\mathbf{ref}}(s)\}. \quad (41)$$

in which $\Gamma\{\cdot\}$ accounts for the cross coupling of $\overline{\boldsymbol{dV}}_{\mathbf{ref}}(\widetilde{s})$ and $\boldsymbol{dV}_{\mathbf{ref}}(\widetilde{s})$ via (39) and (40) with details provided in Appendix A. This coupling could also be considered for the denominator in (38). However, this is not necessary for the investigated case and would only add complexity to the model description.

Finally, a linear equation system describing the primary converter control characteristics can be derived based on (41) and expressed as

$$\mathbf{A}\begin{pmatrix}\square\square\\ \square\square\end{pmatrix} \otimes \underline{x}\begin{pmatrix}\square\\ \square\end{pmatrix} = \underline{B}\begin{pmatrix}\square\\ \square\end{pmatrix}. \quad (42)$$

Details of the model,[7] i.e. the definition of matrix $\mathbf{A}$ and vectors $\underline{B}$ and $\underline{x}$, are provided in the Appendix.

Again, a primary impedance $Z_\mathrm{C}(s) = \frac{\boldsymbol{dV}(s)}{\boldsymbol{di}(s)}$ can be obtained from this description comprising of comparable coupling and disturbance characteristics as for the droop control case. The mirrored component is neglected for any following investigations.

3) ELECTRICAL POWER SYSTEM

The passive electrical grid is modelled based on an equivalent grid impedance

$$Z_\mathrm{grid}(s) = R_\mathrm{grid} + sL_\mathrm{grid}, \quad (43)$$

with an ideal inner sinusoidal voltage source $\boldsymbol{V}_{\mathbf{slack}}(s)$ that is often called a slack node or voltage in power systems.

B. STATE-SPACE MODEL

A detailed model of a linear time-invariant system can be directly derived in time domain by means of the state-space formulation. In contrast to an impedance-based modelling, a stability criterion can be applied to directly determine the global stability based on the state-space model.

These models can include detailed high-order representations of PWM and sampling delays, continuous and discrete controls and highly meshed grid configurations with the disadvantage of substantially increasing the model size. Thus, reduced-order models are often necessary for large-scale power systems to keep the models manageable.

On the flip side, a detailed analysis of the oscillatory system modes and their participating states can be performed providing the possibility to identify main contributors to specific low-damped oscillations [19]. These additional insights can extend the high-order impedance-based stability analysis of large-scale power systems based on a reduced-order state-space model, i.e. only covering the essential states. Analogously, this framework is restricted to the small-signal stability analysis of different operation points.

1) ELECTRICAL STATES

The system under investigation needs to be described by first-order implicit differential equations along with algebraic equations in order to derive a linear state-space model. In case of 3ph power systems, the electrical components are transformed to the dq-frame by $X_\mathrm{dq}(t) = X_{\alpha\beta}(t)e^{-j\omega_0 t}$ with $X_{\alpha\beta}(t) = X_\alpha(t) + jX_\beta(t)$ which yields constant steady-state values by assuming sinusoidal-like transients with the fundamental frequency ω_0.

The considered electrical grid in Section II only consist of the LC filter, the inner converter voltage source $v_\mathrm{inv,dq}(t)$, a grid impedance and the stiff voltage source $v_\mathrm{slack,dq}(t)$. Hence, the six electrical states are defined by the following set of equations:

$$\dot{i}_\mathrm{inv,dq}(t) = \frac{1}{L_\mathrm{f}}\big(v_\mathrm{inv,dq}(t) - v_\mathrm{C,dq}(t) - R_\mathrm{f}i_\mathrm{inv,dq}(t) - j\omega_0 L_\mathrm{f} i_\mathrm{inv,dq}(t)\big), \quad (44)$$

$$\dot{v}_\mathrm{C,dq}(t) = \frac{1}{C_\mathrm{f}}\big(i_\mathrm{inv,dq}(t) - i_\mathrm{grid,dq}(t) - \frac{1}{R_\mathrm{C}}v_\mathrm{C,dq}(t) - j\omega_0 C_\mathrm{f} v_\mathrm{c,dq}(t)\big), \quad (45)$$

$$\dot{i}_\mathrm{grid,dq}(t) = \frac{1}{L_\mathrm{grid}}\big(v_\mathrm{grid,dq}(t) - v_\mathrm{slack,dq}(t) - R_\mathrm{grid}i_\mathrm{grid,dq}(t) - j\omega_0 L_\mathrm{grid} i_\mathrm{grid,dq}(t)\big), \quad (46)$$

where $R_\mathrm{f}/L_\mathrm{f}$ denote the filter inductor resistance and inductance; $R_\mathrm{C}/C_\mathrm{f}$ are the filter capacitor resistance and capacitance; $R_\mathrm{grid}/L_\mathrm{grid}$ are the grid resistance and inductance; $i_\mathrm{inv,dq}(t)$, $v_\mathrm{C,dq}(t)$ and $i_\mathrm{grid,dq}(t)$ are the inverter current, capacitor voltage and grid current in dq-frame, respectively.

2) INNER INVERTER CONTROL STATES

The inner inverter output control algorithms in (17) - (20) need to be transformed to implicit differential equations in the dq-frame. Since the coupling of power-related and fast inner controls which are manifested in the low-frequency range is considered in this work, continuous time representations of the controls are sufficient. Thus, the impedance-based model serves as a highly detailed reference model while the state-space model is reduced to the participating continuous states.

The resonant controllers (17), (18) and (20) are implemented in $\alpha\beta$-frame in order to maintain the positive and negative sequence of the fundamental frequency. Therefore,

[7] The operator $\otimes$ does not simply multiplies a matrix with a vector and is defined in Appendix A.

these controls can be represented by eight states in dq-frame which are defined as

$$\begin{aligned}\dot{X}_{\mathrm{ctrl},1,\mathrm{dq}}(t) = {} & \Delta v_{\mathrm{dif,dq}}(t) - 4\omega_{\mathrm{BW}} X_{\mathrm{ctrl},1,\mathrm{dq}}(t) \\ & -4(\omega_{\mathrm{BW}}^2 + \omega_0^2) X_{\mathrm{ctrl},2,\mathrm{dq}}(t) \\ & -8\omega_{\mathrm{BW}}\omega_0^2 X_{\mathrm{ctrl},3,\mathrm{dq}}(t) \\ & -4\omega_{\mathrm{BW}}^2\omega_0^2 X_{\mathrm{ctrl},4,\mathrm{dq}}(t), \end{aligned} \tag{47}$$

$$\dot{X}_{\mathrm{ctrl},2,\mathrm{dq}}(t) = X_{\mathrm{ctrl},1,\mathrm{dq}}(t), \tag{48}$$

$$\dot{X}_{\mathrm{ctrl},3,\mathrm{dq}}(t) = X_{\mathrm{ctrl},2,\mathrm{dq}}(t), \tag{49}$$

$$\dot{X}_{\mathrm{ctrl},4,\mathrm{dq}}(t) = X_{\mathrm{ctrl},3,\mathrm{dq}}(t), \tag{50}$$

with $\Delta v_{\mathrm{dif,dq}}(t) = \frac{k_{\mathrm{P,V}}}{T_{\mathrm{i,V}}}\big(v_{\mathrm{ref,dq}}(t) - v_{\mathrm{C,dq}}(t)\big)$, exemplarily illustrated for the case of a voltage control loop. The controller bandwidth ω_{BW} and the resonance frequency ω_0 are constant values chosen in the design phase.

The active damping scheme in (19) can be directly derived in the dq-frame based on $i_{\mathrm{C,dq}}(t) = i_{\mathrm{inv,dq}}(t) - i_{\mathrm{grid,dq}}(t)$ with (44), (46) and the general $\alpha\beta$/dq relation $X_{\alpha\beta}(t) = X_{\mathrm{dq}}(t)e^{j\omega_0 t}$ which yields two states

$$\begin{aligned}\dot{v}_{\mathrm{ad,dq}}(t) = {} & K_{\mathrm{rc}}\big(\dot{i}_{\mathrm{C,dq}}(t) + j\omega_0 i_{\mathrm{C,dq}}(t)\big) \\ & -\omega_{\mathrm{rc}} v_{\mathrm{ad,dq}}(t) - j\omega_0 v_{\mathrm{ad,dq}}(t), \end{aligned} \tag{51}$$

where K_{rc} and ω_{rc} denote the proportional gain and bandwidth of the active damping scheme; ω_0 is the steady-state frequency of the linearised operation point.

Considering only a proportional current control loop in (17) in case of a DLVC concept, the controller output can be described by

$$\begin{aligned}v_{\mathrm{ctrl,dq}}(t) = {} & \{k_{\mathrm{P,C}}, 1\}\big(T_{\mathrm{i,V}}\Delta v_{\mathrm{dif,dq}}(t) + 2\omega_{\mathrm{BW}} X_{\mathrm{ctrl},1,\mathrm{dq}}(t) \\ & +4\omega_{\mathrm{BW}}^2 X_{\mathrm{ctrl},2,\mathrm{dq}}(t) + 4\omega_{\mathrm{BW}}\omega_0^2 X_{\mathrm{ctrl},3,\mathrm{dq}}(t) \\ & +4\omega_{\mathrm{BW}}^2\omega_0^2 X_{\mathrm{ctrl},4,\mathrm{dq}}(t) - j2\omega_{\mathrm{BW}}\omega_0 X_{\mathrm{ctrl},2,\mathrm{dq}}(t)\big) \\ & -\{k_{\mathrm{P,C}}, 0\} i_{\mathrm{inv,dq}}(t) - v_{\mathrm{ad,dq}}(t), \end{aligned} \tag{52}$$

where $\{\cdot,\cdot\}$ accounts for the DLVC and SLVC case, respectively.

The PWM and sampling delay characteristics are described by a first-order low-pass filter introducing two additional states:

$$\dot{v}_{\mathrm{inv,dq}}(t) = \frac{1}{T_{\mathrm{d}}}\big(v_{\mathrm{ctrl,dq}}(t) - v_{\mathrm{inv,dq}}(t) - \omega_0 T_{\mathrm{d}} v_{\mathrm{inv,dq}}(t)\big), \tag{53}$$

where T_{d} is the equivalent time delay. Hence, the converter output voltage can be described based on the controls, active damping scheme and the equivalent delays.

In contrast to the impedance model, continuous time equivalents of the control algorithms are used and a first-order approximation of the PWM and sampling delay is introduced. All of these simplifications are negligible in the considered frequency range.

3) POWER-RELATED CONTROL STATES

A small-signal model of the considered system can be derived by linking the inner controls and electrical circuit in (44) - (53) with the dq-equivalents of the non-linear power-related controls in (1) - (7) and conduct the necessary linearisation.

a: DROOP CONTROL

The droop control in (1) - (2) can be described by the following three states

$$\dot{P}_{\mathrm{filt}}(t) = \frac{3}{2}\mathrm{Re}\{v_{\mathrm{grid,dq}}(t)\bar{i}_{\mathrm{grid,dq}}(t)\} - \omega_{\mathrm{LPF}} P_{\mathrm{filt}}(t), \tag{54}$$

$$\dot{Q}_{\mathrm{filt}}(t) = \frac{3}{2}\mathrm{Im}\{v_{\mathrm{grid,dq}}(t)\bar{i}_{\mathrm{grid,dq}}(t)\} - \omega_{\mathrm{LPF}} Q_{\mathrm{filt}}(t), \tag{55}$$

$$\dot{\delta}_{\mathrm{ref}}(t) = \frac{m_\omega}{P_{\mathrm{N}}}\big(P_{\mathrm{filt}}(t) - P_{\mathrm{ref}}(t)\big), \tag{56}$$

with $\hat{V}_{\mathrm{ref}}(t) = \frac{m_{\mathrm{V}}}{P_{\mathrm{N}}}\big(Q_{\mathrm{filt}}(t) - Q_{\mathrm{ref}}(t)\big) + \hat{V}_{\mathrm{N}}$ which is equivalent to a time-domain large-signal representation of (27) and (28). Here, $P_{\mathrm{filt}}(t)/Q_{\mathrm{filt}}(t)$ are the low-pass filtered active and reactive power; ω_{LPF} is the cutoff frequency; $\delta_{\mathrm{ref}}(t)$ is the phase angle of the converter voltage phasor in dq-frame.

It should be pointed out that the non-linear characteristics are introduced by the measured power $S = \frac{3}{2} v_{\mathrm{grid,dq}}(t)\bar{i}_{\mathrm{grid,dq}}(t)$.

b: VIRTUAL OSCILLATOR CONTROL (VOC)

The two states of a virtual oscillator control in (6) - (7) can be expressed as

$$\begin{aligned}\dot{v}_{\mathrm{ref,dq}}(t) = {} & \frac{\zeta}{k_{\mathrm{v}}^2}\left(2V_{\mathrm{N}}^2 - |v_{\mathrm{ref,dq}}(t)|^2\right) v_{\mathrm{ref,dq}}(t) \\ & -j\frac{k_{\mathrm{v}} k_{\mathrm{i}}}{C} i_{\mathrm{grid,dq}}(t) + \frac{2k_{\mathrm{v}} k_{\mathrm{i}} e^{j\varphi}}{3C|v_{\mathrm{ref,dq}}(t)|^2}\overline{S}_{\mathrm{ref}}(t) v_{\mathrm{ref,dq}}(t), \end{aligned} \tag{57}$$

analogously to transforming (38) to the time domain in dq-frame for $\omega_0 = \omega_{\mathrm{N}}$. Again, the convergence speed constant ζ, the scaling factors $k_{\mathrm{v}}/k_{\mathrm{i}}$, the virtual capacitor C and phase angle φ are design parameters.

Here, the non-linear characteristics are introduced by the non-linear control law of the oscillator that includes $|v_{\mathrm{ref,dq}}(t)|^2$.

4) LINEARISATION

Based on (44) - (57), the system equations can be generally expressed as

$$\dot{x}(t) = f\big(x(t), u(t)\big), \tag{58}$$

with the system states $x(t) = \{x_1(t), \ldots, x_n(t)\}$ and the system input $u(t) = v_{\mathrm{slack}}(t)$.

Linearisation of the power-related control is necessary in order to perform a stability analysis in state space. In general, small-signal perturbations of the states $x(t)$ can be described by the first-order approximation

$$\Delta\dot{x}(t) = \left.\frac{\partial f\big(x(t)\big)}{\partial x(t)^{\mathrm{T}}}\right|_{x_0} \Delta x(t), \tag{59}$$

where the system steady state is defined by x_0.[8]

[8] Small-signal variables are expressed by lower-case letters with Δ in front of the letters, steady-state variables are denoted with lower-case letters as well but with a "0" in the subscript.

This provides the possibility to formulate the small-signal model as vectors and matrices:

$$\Delta\dot{\underline{x}}(t) = \mathbf{A}\Delta\underline{x}(t) + \mathbf{B}\Delta\underline{u}(t), \tag{60}$$
$$\Delta\underline{y}(t) = \mathbf{C}\Delta\underline{x}(t) + \mathbf{D}\Delta\underline{u}(t), \tag{61}$$

consisting of the state matrix **A**, the input matrix **B**, the output matrix **C** and the feed-forward matrix **D**.

Here, the state vector is exemplarily listed for a VOC-controlled converter with an inner DLVC concept:

$$\Delta\underline{x}(t) = \big[\Delta i_{\mathrm{inv,dq}}(t),\, \Delta v_{\mathrm{C,dq}}(t),\, \Delta i_{\mathrm{grid,dq}}(t),\, \Delta v_{\mathrm{ad,dq}}(t),\, \Delta X_{\mathrm{ctrl,1-4,dq}}(t),\, \Delta v_{\mathrm{ref,dq}}(t),\, \Delta v_{\mathrm{inv,dq}}(t)\big]^{\mathrm{T}} \tag{62}$$

In addition, the state vector of a droop-controlled converter with an inner DLVC concept can be described by

$$\Delta\underline{x}(t) = \big[\Delta i_{\mathrm{inv,dq}}(t),\, \Delta v_{\mathrm{C,dq}}(t),\, \Delta i_{\mathrm{grid,dq}}(t),\, \Delta v_{\mathrm{ad,dq}}(t),\, \Delta X_{\mathrm{ctrl,1-4,dq}}(t),\, \Delta P_{\mathrm{filt}}(t),\, \Delta Q_{\mathrm{filt}}(t),\, \Delta\delta_{\mathrm{ref}}(t),\, \Delta v_{\mathrm{inv,dq}}(t)\big]^{\mathrm{T}}. \tag{63}$$

The system input is identically defined for all cases as

$$u(t) = \big[\Delta v_{\mathrm{slack,dq}}(t)\big]^{\mathrm{T}}. \tag{64}$$

More details are provided in Appendix B and are published for similar grid-forming setups with different objectives in [18], [45].

C. PHASE PORTRAIT MODEL

The ability of a cluster of voltage sources, e.g. synchronous generators or grid-forming converters, to remain synchronised during severe disturbances is part of the transient stability analysis. In case of grid-forming converters, the power-related controls are responsible for the synchronisation. Phase portraits of the considered systems can be used to investigate theses events. In particular, the phase-portrait analysis is an indirect stability assessment in time domain for large-signal aspects [8] and has already been applied to droop-controlled converter systems [17].

In order to perform this analysis, reduced-order models need to be derived. In addition, this approach is limited to analyse specific large-signal events while analytical solutions are often difficult to acquire. Thus, a numerical integration can be necessary in order to perform a graphical evaluation of the $\dot{\delta} - \delta$ curve, which is the so-called phase portrait [17].

In general, this framework provides the possibility to investigate special events like a severe voltage sag in a design-oriented analysis due to the ability to cover large-signal transients. Hence, this method extends the previously described small-signal analysis concepts.

1) STATIC PHASOR-BASED MODELLING

Some basic properties of the synchronisation-related transients are assumed in the conventional phase-portrait analysis, namely: (a) all relevant transients can be represented by phasors of the fundamental frequency (slowly varying sinusoidal signals); the electrical power system can be represented by static impedances and admittances (states of e.g. the transmission lines and transformers are not participating in the relevant modes); (c) the inner converter controls can be neglected due to their fast nature; (d) only the power-related control states are taken into account. These assumptions lead to similar simplifications as for the quasi-steady state concept used in power system simulations.

Therefore, the droop-controlled converter setup in Fig. 1 can be described by the non-linear set of equations in (54) - (56) combined with the Thévenin equivalent of the electrical grid which yield

$$\ddot{\delta}(t) = -\omega_{\mathrm{LPF}}\dot{\delta}(t) - m_{\omega}\omega_{\mathrm{LPF}}\Bigg(-\frac{3X_{\mathrm{grid}}}{2|Z_{\mathrm{grid}}|^2}E(t)V(t)\sin\delta(t) + P_{\mathrm{ref}}(t) - \frac{3R_{\mathrm{grid}}}{2|Z_{\mathrm{grid}}|^2}\big(V(t)^2 - V(t)E(t)\cos\delta(t)\big)\Bigg), \tag{65}$$

$$\dot{V}(t) = \omega_{\mathrm{LPF}}(\hat{V}_{\mathrm{N}} - V(t)) - m_{\mathrm{V}}\omega_{\mathrm{LPF}}\Bigg(\frac{3R_{\mathrm{grid}}}{2|Z_{\mathrm{grid}}|^2}E(t)V(t)\sin\delta(t) + Q_{\mathrm{ref}}(t) - \frac{3X_{\mathrm{grid}}}{2|Z_{\mathrm{grid}}|^2}\big(V(t)^2 - V(t)E(t)\cos\delta\big)\Bigg), \tag{66}$$

with $V(t) = |\boldsymbol{V}_{\mathbf{PCC}}(t)|$, $E(t) = |\boldsymbol{V}_{\mathbf{slack}}(t)|$
and $\delta(t) = \angle\{\boldsymbol{V}_{\mathbf{PCC}}(t) - \boldsymbol{V}_{\mathbf{slack}}(t)\}$.

Here, phasors are indicated by bold symbols and $\boldsymbol{V}\angle\boldsymbol{\delta}$ is the voltage phasor at the PCC which is equivalent to the inner droop control voltage phasor in (1) - (2). A similar model is derived in Appendix C for a VOC-controlled converter.

This basic model has recently been used to investigate the droop control for short-circuit aspects [17]. However, the coupling of the electrical grid with the inner and outer control loop in the power-related frequency range is considered in this work. Since these aspects are classically neglected, an extension covering these aspects is presented in the next section.

2) DYNAMIC PHASOR-BASED MODELLING

The relevant couplings of the investigated scenario can be included in (65) - (66) and in Appendix C by introducing an extensions to include (a) all electrical states and (b) the inner control states. Thus, the model can no longer be described by a first- or second-order non-linear differential equation so that the stability analysis is performed based on a reduced-order time-domain simulation framework rather than by graphically analysing the trajectory in the phase plane.

However, this trajectory can still impressively illustrate the oscillatory modes as in Fig. 6, even though the limits of this analysis technique are reached.

a: ELECTRICAL STATES

The concept of dynamic phasors of the fundamental frequency is suitable to represent the aspects of dynamically changing sinusoidal signals due to the electrical grid [46]. Therefore, all inductors and capacitors in the electrical circuit

need to be described by

$$\boldsymbol{V}_{\mathbf{L}}(t) = R\boldsymbol{I}_{\mathbf{L}}(t) + L\dot{\boldsymbol{I}}_{\mathrm{L}}(t) + j\omega_0 L\boldsymbol{I}_{\mathbf{L}}(t), \tag{67}$$

$$\boldsymbol{I}_{\mathbf{C}}(t) = \frac{\boldsymbol{V}_{\mathbf{C}}(t)}{R} + C\dot{\boldsymbol{V}}_{\mathrm{C}}(t) + j\omega_0 C\boldsymbol{V}_{\mathbf{C}}(t). \tag{68}$$

On a side note, this concept is also used by the power system community when deriving a state-space model of electrical grids in dq-frame, i.e. in (44) - (46). If a specific harmonic content is of interest, one may include multiple dynamic phasors analogously to the study case in [47].

b: INNER INVERTER OUTPUT CONTROL

The inner controls can be easily included using (50) - (53) transformed to a phasor representation $\boldsymbol{X}(t) = X_{\mathrm{d}}(t) + jX_{\mathrm{q}}(t)$. Thus, the final model is equivalent to the large-signal dq-frame state-space model in (58) which needs numerical integration of specific study cases in order to evaluate stability aspects. A direct stability assessment based on the eigenvalues is not applicable due to the non-linear nature.

In addition, illustration of the complete equation system is omitted for the sake of brevity.

IV. ANALYSIS OF SYSTEM CHARACTERISTICS

The previously derived models serve as a basis to investigate interactions between the inner and outer control loops via the electrical grid in case of the setup illustrated in Fig. 1.

In addition, correlations between the different modelling frameworks are studied in order to guarantee a consistent modelling.

A. IMPEDANCE-BASED ANALYSIS

The setup in Fig. 1 can be represented in the impedance-based framework by coupling the converter impedance $Z_{\mathrm{C}}(s)$ with the grid impedance $Z_{\mathrm{grid}}(s)$ which yields the so-called minor feedback $\mathrm{NY} = Z_{\mathrm{C}}(s)/Z_{\mathrm{grid}}(s)$ [48]. In addition, a generalised framework is proposed in [23] enabling the possibility to create impedance equivalents for large-scale power systems. In order to analyse the local stability, the Nyquist criterion can be applied to the models, specified in the Appendix, which is illustrated in Fig. 4 by a Nyquist plot for each inner control setup in positive-sequence domain.

In general, the minimal distance η_{h} to the critical point $\times = -1 + j0$ (Nyquist criterion) is illustrated in Fig. 4 by black arrows indicating that no instability occurs for all variations. However, modes with low damping η_{h} can be identified in the high-frequency range and power-related frequency range depending on the control concept. The high-frequency characteristics of the VOC- and droop-controlled converter are identical (blue line overlaps the red one for $f > 500\,\mathrm{Hz}$ in Fig. 4) and are beyond the scope of this work. Thus, η_{h} is only evaluated for the low frequency range of $f \approx 0 - 150\,\mathrm{Hz}$.

In particular, potentially power-related modes with a resonance frequency $f_{\mathrm{h}} \approx 26.5 - 31.9\,\mathrm{Hz}$ and a low damping, i.e. minimal distance $\eta_{\mathrm{h}} \approx 0.29 - 0.54$, can be identified

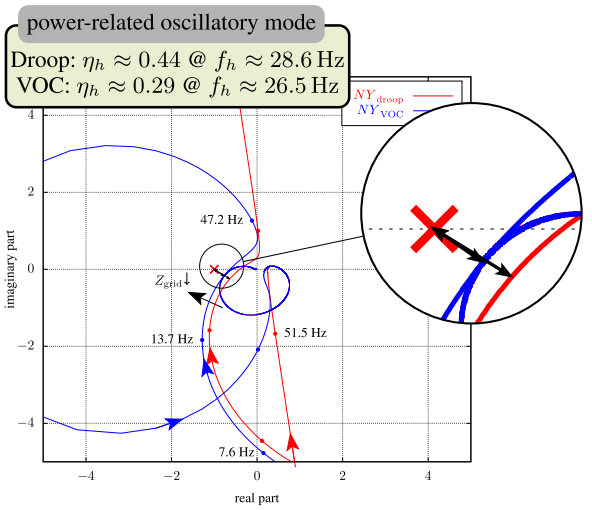

(a) Nyquist plot for the dual loop voltage control

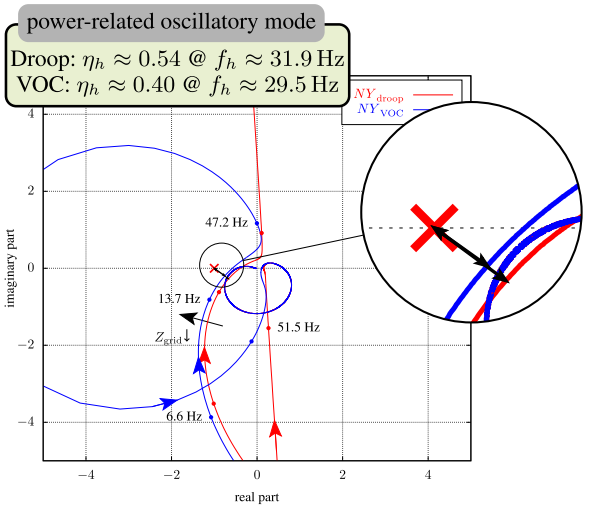

(b) Nyquist plot for the single loop voltage control

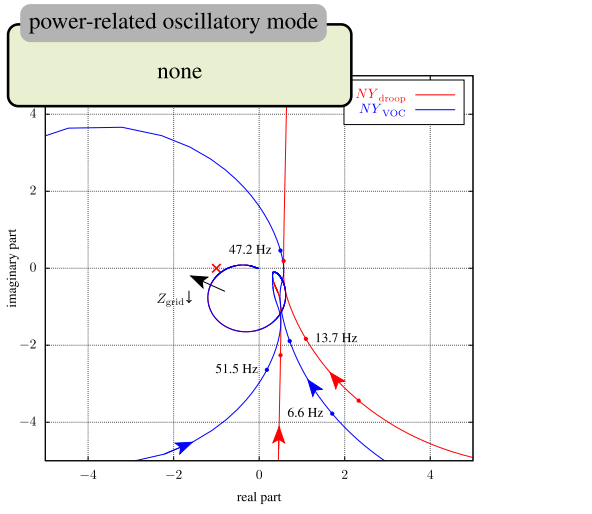

(c) Nyquist plot for the open loop voltage control

FIGURE 4. Stability Analysis of the considered system, whose parameters are listed in Table 2: Nyquist criterion applied to the quotient of the converter impedance $Z_{\mathrm{C}}(s)$ and the impedance of the electrical grid $Z_{\mathrm{grid}}(s)$ in positive sequence denoted as NY; considered power-related frequency range: $f \approx 0 \ldots 150\,\mathrm{Hz}$.

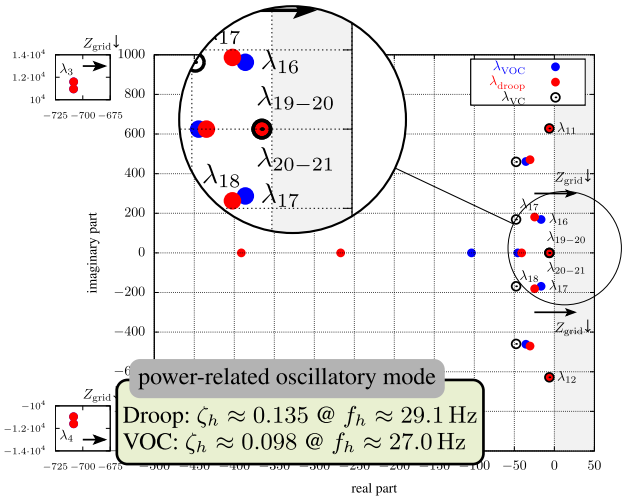

(a) Eigenvalues for dual loop voltage control

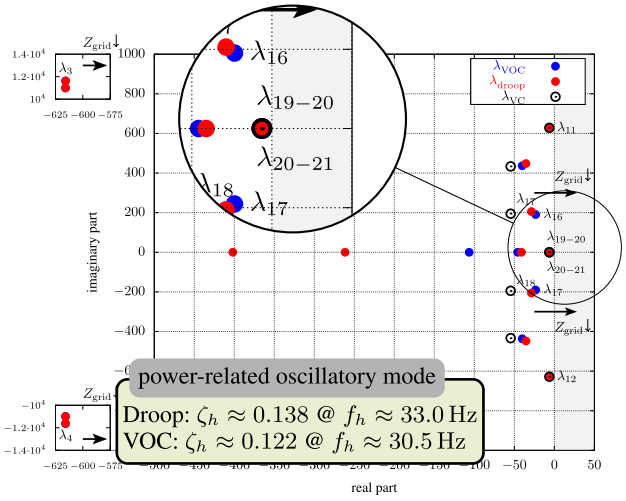

(b) Eigenvalues for single loop voltage control

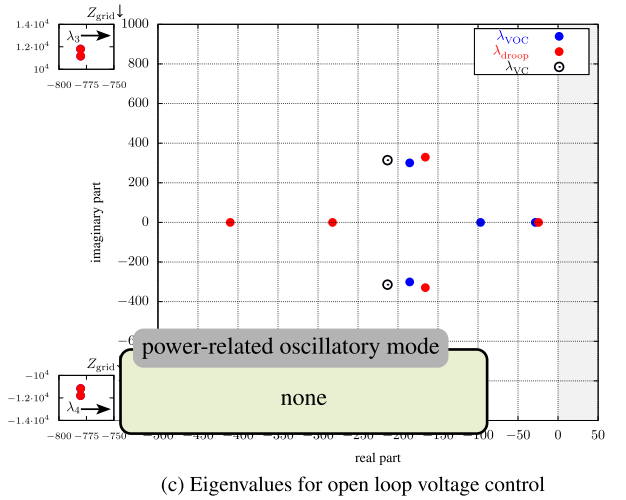

(c) Eigenvalues for open loop voltage control

FIGURE 5. Stability Analysis of the considered system, whose parameters are listed in Table 2: analysis of the power-related eigenvalues λ of the system matrix A for VOC, droop and a basic voltage control (VC); considered power-related frequency range: $f \approx 0 \ldots 150$ Hz.

for the DLVC and SLVC concept.[9] In this case, the relatively small (inductive) grid impedance contributes to this mode. Thus, reducing the grid impedance Z_{grid} shifts the Nyquist plots towards the critical point $\times$ which highlights the high burden that is imposed on voltage-controlled entities by small terminal impedances. The impact of Z_{grid} on the minor feedback is illustrated by a black arrow in Fig. 4. These results are in line with the analysis in [32], [49], which is based on simplified transfer functions[10] in order to tune the dynamic performance and derive necessary and sufficient constraints for the droop and line parameters. Furthermore, the droop control comprises a slightly higher damping compared to the VOC concept while the resonance frequency is also slightly higher. The OLVC curve does not indicate any potential oscillations in the power-related frequency range. However, the damping of the high-frequency resonance is lower in this case due to the missing inner current and/or voltage control which introduces additional damping.

In conclusion, only the coupled consideration of the inner control, the electrical grid and the power-related control reveals an oscillatory mode in the power-related frequency range with low damping.

B. STATE-SPACE EIGENVALUES

The system stability can be analysed in the state-space framework by the eigenvalues λ of the system matrix $\mathbf{A}$. These eigenvalues are equivalent to the system modes providing a possibility to directly identify oscillatory modes. The results of the investigated scenario are shown in Fig. 5 for all variations.

In general, the four modes of the $\alpha\beta$-frame resonant controllers can be identified (here: $f_{19,20}/f_{20,21} \approx 0$ Hz and $f_{11,12} \approx 100$ Hz) for DLVC and SLVC which are intended to oscillate and, thus, will not shift towards the unstable region. In addition, the power-related modes $\lambda_{16-17}/\lambda_{17-18}$ are much closer (at least one order of magnitude) to the imaginary axis (instability) than the high-frequency ones λ_{3-4}, i.e. located outside of the main plot range. Both pairs of eigenvalues will shift towards the imaginary axis when the grid impedance $Z_{\text{grid}}(s)$ is reduced which is indicated by a black arrow in Fig. 5.The most relevant modes are also listed in Table 1. Based on their locations and participating states, the high-frequency modes will probably not be excited despite their low damping ζ_h.[11]

[9]The general Nyquist criterion for multivariable systems in [44] yields $f_{\text{h}} \approx 26.6 - 32.6$ Hz and $\eta_{\text{h}} \approx 0.29 - 0.61$ which justifies applying the characteristic SISO impedances.

[10]A time scale separation of the outer and inner control loop is assumed and validated for the investigated case such that the inner control can be neglected.

[11]The damping factor is defined as $\zeta_h = -\frac{\text{Re}\{\lambda\}}{|\lambda|}$ and is not identical to the minimal distance η_{h} that can serve as an indication for oscillatory modes in an impedance-based framework. However, a comparison of the damping performance across the different converter variations based on these indicators can be done in order to verify the equivalence of both models.

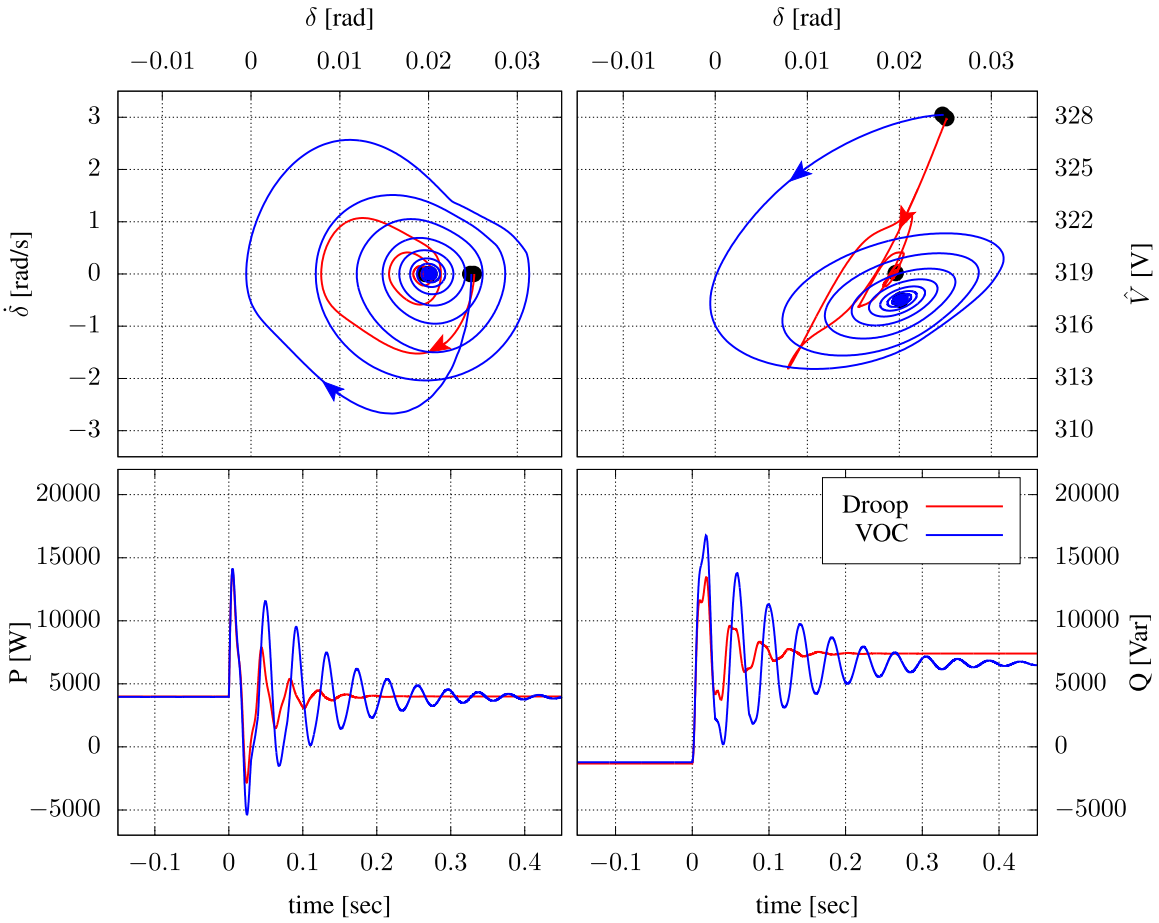

FIGURE 6. Stability Analysis of the considered system, whose parameters are listed in Table 2: phase portrait of the transient response to a voltage step from 1 pu to 0.92 pu; example case for the dual loop voltage control concept; δ denotes the inner voltage phase angle, $\hat{V}$ is the voltage amplitude and P/Q are the active and reactive power.

In particular, the power-related modes $\lambda_{16-17}/\lambda_{17-18}$ with $f_\mathrm{h} \approx 27 - 33\,\mathrm{Hz}$ are closest to the unstable region, comprise a low damping factor $\zeta_\mathrm{h} \approx 0.098 - 0.138$ and will probably oscillate when excited by a transient event. Furthermore, the droop-controlled converter includes a slightly higher damping and natural frequency consistently with the impedance-based results. The grid-forming converters with a SLVC concept are marginally better damped. Again, the OLVC concept does not introduce insufficiently damped power-related modes.

In addition, a modal analysis based on the participation factors[12] of each state to the oscillatory modes has been performed and is listed in Table 1. In general, this enables a systematic analysis of the system states which are major participants to the relevant modes. It can be identified that the power-related oscillatory modes $\lambda_{16-17}/\lambda_{17-18}$ are manifested by the main coupling of the grid current $i_\mathrm{grid,dq}$ (state of L_grid), the inner controls $\mathrm{VC}_\mathrm{st,dq}$ and the power-related control $\mathrm{PC}_\mathrm{st,dq}$. The state matrix $\boldsymbol{A}$ describes this coupling effect and is listed in Appendix B. Thus, these stability aspects are not covered if one of the identified states is missing or not modelled. In contrast, the high frequency modes λ_{3-4} are mostly based on the LCL resonances coupled with the inner converter control.

In conclusion, only small deviations regarding the natural frequency f_h or the damping performance ζ_h are identified between state-space eigenvalues and the impedance-based analysis. In addition, the participation analysis provides additional insights of the coupling path.

C. PHASE PORTRAIT

Numerical integration of the phase-portrait model in Section III-C provides the possibility to investigate specific large-signal events in the time domain. Here, the transient response of a droop-controlled converter and a VOC-controlled converter, both based on the DLVC concept, are exemplarily shown in Fig. 6 for a voltage step from 1 pu to 0.92 pu. Both systems start in the steady state that is defined by the voltage phasor marked by a black point in Fig. 6. At time $t = 0\,\mathrm{s}$, the voltage step occurs which results in a new steady-state voltage phasor (indicated by a second black

[12]The participation factors are defined as $\mathrm{PF}_{ki} = \frac{|\boldsymbol{V}(k,i)\boldsymbol{W}(k,i)|}{|\boldsymbol{W}(i,:)||\boldsymbol{V}(:,i)|}$ with the matrices that contain the left and right eigenvectors $\boldsymbol{V}$ (column vectors) and $\boldsymbol{W}$ (row vectors), respectively.

TABLE 1. State-Space Analysis: Most Relevant Oscillatory Modes λ and Participation Factors PF.

		droop control		VOC	
	SYMBOL	λ_{17-18}	λ_{3-4}	λ_{16-17}	λ_{3-4}
DLVC	$\mathrm{PF}_{\mathrm{E_{st,dq}}}$	30%	92%	36%	92%
	$\mathrm{PF}_{\mathrm{VC_{st,dq}}}$	57%	8%	53%	8%
	$\mathrm{PF}_{\mathrm{PC_{st}}}$	12%	0%	13%	0%
	f_h	29.1 Hz	1848 Hz	27 Hz	1848 Hz
	ζ_h	0.135	0.061	0.098	0.061
	$\mathrm{Re}\{\lambda_\mathrm{h}\}$	-24.7	-708	-16.6	-708
SLVC	$\mathrm{PF}_{\mathrm{E_{st,dq}}}$	33%	92%	36%	92%
	$\mathrm{PF}_{\mathrm{VC_{st,dq}}}$	56%	8%	52%	8%
	$\mathrm{PF}_{\mathrm{PC_{st}}}$	11%	0%	11%	0%
	f_h	33.0 Hz	1852 Hz	30.5 Hz	1852 Hz
	ζ_h	0.138	0.053	0.122	0.053
	$\mathrm{Re}\{\lambda_\mathrm{h}\}$	-28.7	-616	-23.3	-616
OLVC	$\mathrm{PF}_{\mathrm{E_{st,dq}}}$	-	95%	-	95%
	$\mathrm{PF}_{\mathrm{VC_{st,dq}}}$	-	5%	-	5%
	$\mathrm{PF}_{\mathrm{PC_{st}}}$	-	0%	-	0%
	f_h	-	1882 Hz	-	1882 Hz
	ζ_h	-	0.066	-	0.066
	$\mathrm{Re}\{\lambda_\mathrm{h}\}$	-	-780	-	-780

The electrical states are named as $\mathrm{E_{st,dq}}$; voltage control states denoted as $\mathrm{VC_{st,dq}}$ and power control states denoted as $\mathrm{PC_{st}}$; f_h is the natural frequency and ζ_h is the damping factor.

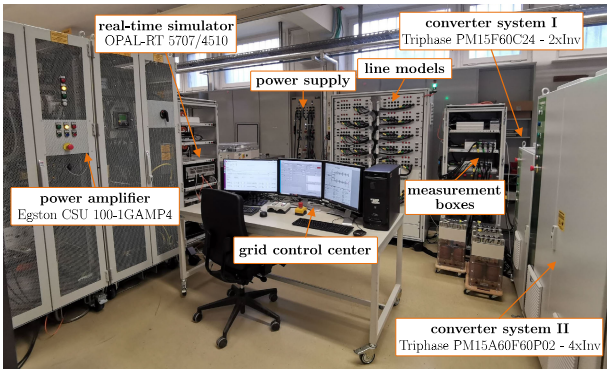

FIGURE 7. IAL Microgrid: photograph of the laboratory setup.

point). This time, the steady-state voltage phasors differ for the droop control and VOC according to (1) - (2) and (11) - (12).

The transient response in Fig. 6 confirms the low-frequency oscillatory mode manifested in the active and reactive power (respectively in the voltage phasor $\hat{V}\angle\delta$) with $f \approx 27 - 29\,\mathrm{Hz}$. The droop-controlled converter comprises a better damping which is consistent with the small-signal analysis. In addition, the high-frequency mode is not excited. The numerical simulation of the other controls validate the small-signal stability analysis equivalently and are not shown here for the sake of brevity.

In conclusion, identical results can be obtained with all three model frameworks since the relevant coupling path of the power-related oscillatory modes are included in each model. In particular, the considered study case of a voltage step from 1 pu to 0.92 pu, even being outside of the small-signal region, yields similar oscillations as elaborated for the impedance- and state space-based analysis.

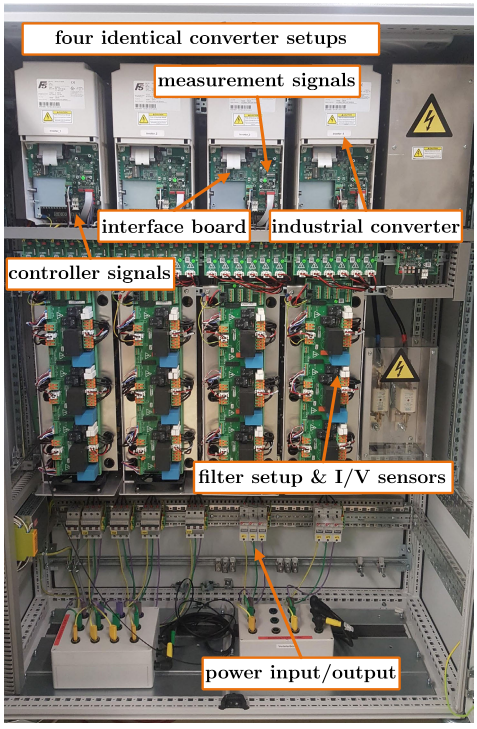

FIGURE 8. IAL Microgrid: photograph of the converter system II.

V. EXPERIMENTAL VALIDATION

This section extends and validates the previously conducted analysis by laboratory experiments with regard to the impedance-based models and the excitation of oscillatory modes during transients.

A. LABORATORY SETUP

The laboratory experiments have been performed at the IAL Microgrid test bench with the basic setup shown in Fig. 7. This configuration provides the possibility to analyse a variety of different converter-related aspects based on two Triphase converter systems PM15, each consisting of up to four programmable inverters with a rated power of $S_\mathrm{N} = 16\,\mathrm{kVA}$ and a switching frequency of $f_\mathrm{s} = 16\,\mathrm{kHz}$, that can be equipped with LC or LCL filters and custom control algorithms. In addition, a four-quadrant digital power amplifier Egston CSU 100 ($S_\mathrm{N} = 100\,\mathrm{kVA}$, $f_\mathrm{s} = 125\,\mathrm{kHz}$) can be used in combination with two OPAL-RT real-time simulators OP5707/OP4510 in order to establish a power-hardware-in-the-loop setup. Additional equipment can be used to create a small electrical grid and to obtain synchronised measurements of different nodes.

All of the the considered grid-forming control concepts are each implemented on one converter of the converter system II in Fig. 8 (rated current $I_\mathrm{N} = 24\,\mathrm{A}$, rated voltage $V_\mathrm{N} = 400\,\mathrm{V}$) based on the parameters listed in Table 2. The combination of power amplifier and real-time simulator is operated in one of two modes: (1) as an ideal current source directly connected to the Triphase system in order to extract the

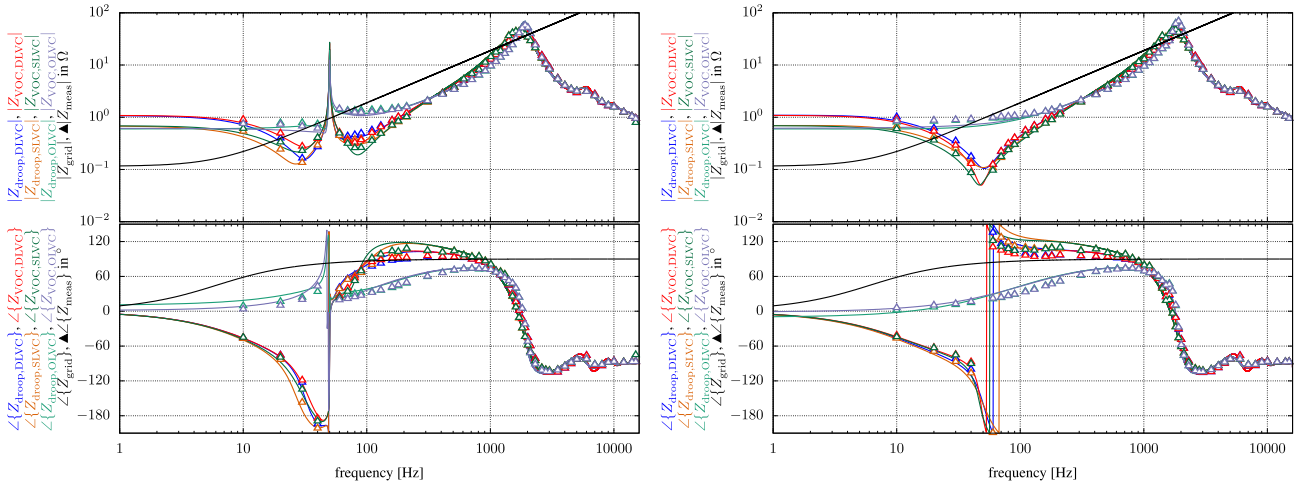

(a) positive-sequence impedance (b) negative-sequence impedance

FIGURE 9. Experimental validation of sequence impedance characteristics of the considered converter systems, whose parameters are listed in Table 2: frequency sweep from 1 Hz to 16 kHz for positive- and negative-sequence impedance of VOC-controlled converter $Z_{\mathrm{VOC}}(s)$, droop-controlled converter $Z_{\mathrm{droop}}(s)$, the passive grid $Z_{\mathrm{grid}}(s)$ and experimental results $Z_{\mathrm{meas}}(s)$; the dual loop, single loop and open loop voltage control is considered as inner control setup.

converter impedance by introducing a steady-state operation point with a small-signal current disturbances; (2) as an ideal voltage source connected to the Triphase system via the grid inductor to be able to obtain the transient response to a voltage step. Either way, the measurements are performed using three Testec TT SI9110 voltage probes (100 MHz/1000 Vrms AC/2% accuracy) and three Keysight N2783B current probes (100 MHz/30 Arms AC/1% accuracy) linked to an LeCroy HDO8108A oscilloscope (sampled with 1 MHz).

B. EVALUATION OF STEADY-STATE IMPEDANCE MODELS

A frequency sweep is performed based on the previously described setup in order to extract the small-signal characteristics of all considered grid-forming concepts. The procedure to obtain these impedances is defined as: (1) VOC- or droop-controlled converter: start operation; (2) power amplifier: synchronisation; (3) power amplifier: set steady state; (4) power amplifier: transition from PLL-based to current mode with $f = f_{\mathrm{N}}$; (5) power amplifier: injection of a perturbation and (6) data acquisition. In order to obtain a high accuracy, five measurements are performed for each frequency. A small standard deviation ($\approx 2\%$ of mean value; within the range of the measurement accuracy) is achieved with this procedure indicating a high confidence in the measurement results. Hence, only the average for each frequency is used further.

The phase-domain impedance models are compared with experimental results separately for positive and negative sequence as amplitude and phase in Fig. 9 without error bars. The grid impedance of the considered setup is shown as a reference. It can be identified that the DLVC and SLVC concept are nearly identical based on the fact that the inner current control loop only adds additional damping due to the non-existing integrator and similar control gains. In addition, these concepts introduce either a capacitive ($f < f_0$) or inductive ($f > f_0$) characteristic in the power-related frequency range of $f \approx 0 - 150$ Hz that is more likely to interact with the grid impedance towards low-damped oscillatory modes. In particular, the combination of power-related control and the integrator of the inner control loop cause this characteristic which is typical for all popular grid-forming control concepts (e.g. VSG, Synchronverter, droop and matching control) due to their similar feedback characteristics [31], [40], [48], [50]. Here, the capacitive case below $f = f_0$ is critical. In case of coupling with another grid-feeding converter, a critical mode for the inductive case above $f = f_0$ can also arise, i.e. in [14]. As a side note, the capacitive case is typically avoided or managed by adding an inductive virtual impedance in the controls as elaborated for the context of robust stability analysis in [38]. The impact of the power-related control in Fig. 9 is mostly restricted to the positive-sequence characteristics. The OLVC concept introduces a marginally larger impedance with inductive characteristics close to the fundamental frequency which is mostly based on the LC filter parameters. In general, only minor deviations are identified confirming a high model fidelity.

C. EVALUATION OF TRANSIENT RESPONSE

The different grid-forming converters are coupled with an external grid based on the previously described setup in order to obtain the transient response to a voltage step from 1 pu to 0.92 pu. The response is extracted by applying a specific procedure: (1) power amplifier: start external grid; (2) VOC- or droop-controlled converter: start operation and synchronisation; (3) VOC- or droop-controlled converter: adjust reference values to meet the steady state in Table 2; (4) power amplifier: dictate a voltage step. The measured and simulated active and reactive power of the VOC- and droop-controlled

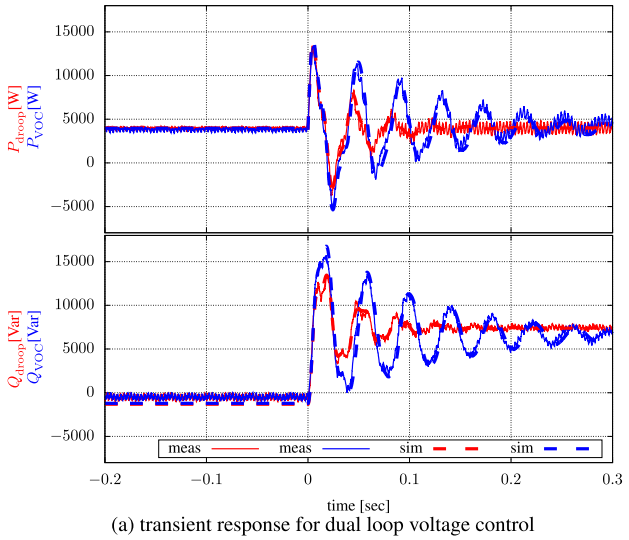

(a) transient response for dual loop voltage control

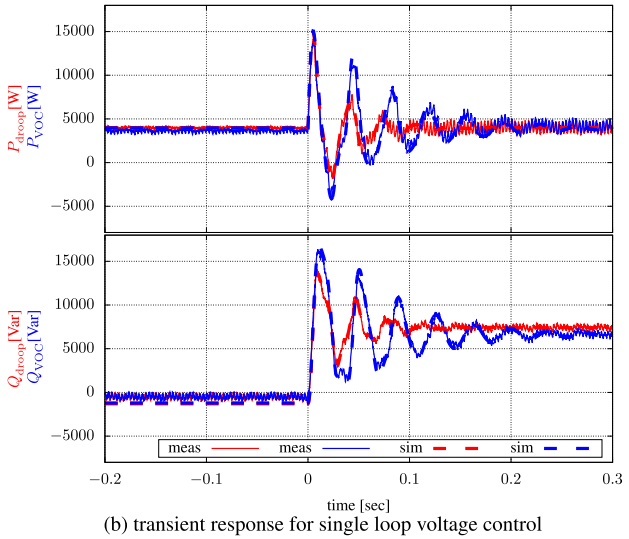

(b) transient response for single loop voltage control

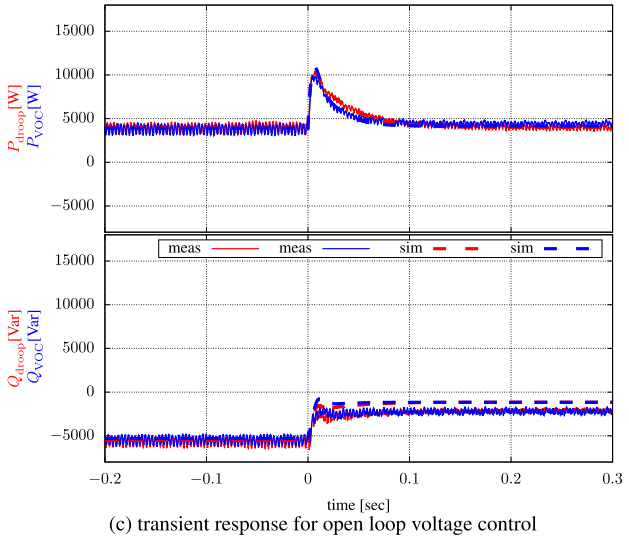

(c) transient response for open loop voltage control

FIGURE 10. Experimental validation of the transient response of the considered systems, whose parameters are listed in Table 2: voltage step from 1 pu to 0.92 pu; measured active and reactive power (meas) are illustrated by solid lines, simulated power (sim) are illustrated by dashed lines.

converter is illustrated in Fig. 10 for all control variations. The simulation is based on the phase-portrait models.

At $t = 0$ s, the magnitude of the slack voltage $\hat{V}_{\text{slack}}$ (inner grid voltage or voltage of the power amplifier) drops from 1 pu to 0.92 pu, which ultimately yields a new steady state operation point. Due to the non-negligible reactive power flow, the steady-state reference voltage phasors $\underline{V}_{\mathbf{ref}}$ and consequently the operation points of the VOC- and droop-controlled converter are no longer identical based on the outer control equations (1) - (2) and (11) - (12). In case that an inner control loop is used (Fig. 10-a and -b), an insufficiently damped oscillation of the active and reactive power can be identified. In particular, the predicted oscillatory modes are excited with correct damping relations between DLVC and SLVC concept. In addition, the resonance frequencies match the results obtained by the small-signal stability analysis. If the inner controller is omitted (Fig. 10-c), the preferable first-order low-pass behaviour of grid-forming converters occurs. Hence, the OLVC concept contains no insufficiently damped oscillatory modes in this study case. The MWE confirms the potentially high burden that is imposed on the voltage control by the coupling of grid-forming converters with a relative small inductive impedance. Again, small refers to the converter impedance at the oscillatory mode.

In general, the high model fidelity of the impedance-based models is also verified for the state-space and phase-portrait models.

VI. CONCLUSION

In this article, the coupling of inner control loops with the power-related control in grid-forming power converters via the grid states has been comprehensively investigated by the impedance-based, state-space and phase portrait-based framework for a minimal working example. Besides its basic effects, the explicit coupling path is elaborated. Furthermore, this analysis is validated by extensive laboratory experiments.

In particular, interactions of the inner and outer control loops of grid-forming converter can occur for low-impedance scenarios which need to be covered in a comprehensive power system stability assessment. For this purpose, the inner control and grid states need to be modelled. In time-domain simulations, this can be achieved by e.g. the dynamic phasor concept. In frequency domain, detailed impedance-based models can be combined towards a representation of the power system. Conventional approaches, like a quasi-steady state model, are missing these modes. Furthermore, the superior bandwidth of a VOC compared to the conventional droop control yields a stronger coupling with the inner control for the investigated scenarios. Thus, oscillations with less damping occur for this setup.

In conclusion, detailed converter models can be necessary even for the analysis of power-related transients in large-scale converter-dominated power systems which requires suitable methods to limit the computational burden. Due to its modularity, the impedance-based framework is one of the preferred

solutions that enables the analysis of small-signal stability aspects. Among the published work in this area, the concept of a generalised impedance-based framework, that allows a systematic stability assessment of large-scale deterministic power systems, can effectively reveal stability issues in converter-dominated power systems.

APPENDIX A
IMPEDANCE MODELS

The steady-state impedance characteristics of a droop-controlled converter can be described by the equation system on the next page with the impedance and closed loop TF of the inner control loop $Z_C(s)$ and $G_{cl}(s)$, respectively.

Furthermore, the equivalent impedance of a VOC-controlled converter can be derived based on the equations (X) where $A_{j,k}$ is the matrix entry in the j-th row and k-th column and x_i is the i-th vector entry. The notation $\bar{x}_1$ defines the conjugate complex of x_1. This representation can be merged with the inner converter controls that yields $Z_{VOC,DLVC}(s) = \underline{x}_1 G_{cl,DLVC}(s) + Z_{C,DLVC}(s)$ for the case of a dual loop voltage controlled-converter.

APPENDIX B
STATE-SPACE MODELS

The investigated state-space model is exemplarily listed for a dual loop voltage control concept. The individual couplings between different states can be illustrated by the following submatrices.

a: ELECTRICAL STATES

Contribution to own states:

$$\mathbf{A}_{el} = \begin{bmatrix} -\kappa_1\mathbf{I} - \omega_0\mathbf{D}_- & -\frac{1}{L_f}\mathbf{I} & \mathbf{0}_2 \\ \frac{1}{C_f}\mathbf{I} & -\kappa_2\mathbf{I} - \omega_0\mathbf{D}_- & -\frac{1}{C_f}\mathbf{I} \\ \mathbf{0}_2 & \frac{1}{L_{grid}}\mathbf{I} & -\kappa_3\mathbf{I} - \omega_0\mathbf{D}_- \end{bmatrix}$$

Contribution to other states:

$$\mathbf{A}_{el/ad} = K_{rc}\left[-(\kappa_1+\kappa_2)\mathbf{I}\ (\kappa_2^2-\kappa_4)\mathbf{I}\ (\kappa_3+\kappa_2)\mathbf{I}\right]$$

$$\mathbf{A}_{el/ctrl} = \begin{bmatrix} \mathbf{0}_{2\times2} & -\frac{k_{P,V}}{T_{i,V}}\mathbf{I} & \mathbf{0}_{2\times2} \\ \mathbf{0}_{6\times2} & \mathbf{0}_{6\times2} & \mathbf{0}_{6\times2} \end{bmatrix}$$

$$\mathbf{A}_{el/droop} = \frac{3}{2}\omega_{LPF}\begin{bmatrix} \mathbf{0}_{1\times2} & i_{grid,d,0}\mathbf{I} - i_{grid,q,0}\mathbf{D}_- & v_{C,q,0}\mathbf{D}_+ + v_{C,d,0}\mathbf{I}^* \\ \mathbf{0}_{1\times2} & \mathbf{0}_{1\times2} & \mathbf{0}_{1\times2} \end{bmatrix}$$

$$\mathbf{A}_{el/d} = \begin{bmatrix} -\frac{k_{P,C}}{T_d}\mathbf{I} & -\frac{k_{P,C}k_{P,V}}{T_d}\mathbf{I} & \mathbf{0}_{2\times2} \end{bmatrix}$$

with $\kappa_1 = \frac{R_f}{L_f}$, $\kappa_2 = \frac{1}{CR_C}$, $\kappa_3 = \frac{R_{grid}}{L_{grid}}$, $\kappa_4 = \frac{1}{L_{grid}} + \frac{1}{L_f}$ zero matrix $\mathbf{0}$, anti-diagonal matrix $\mathbf{D}_- = \text{adiag}(-1, 1)$/$\mathbf{D}_+ = \text{adiag}(1, 1)$ and identity matrix $\mathbf{I} = \text{diag}(1, 1)$/$\mathbf{I}^* = \text{diag}(1, -1)$

TABLE 2. Experimental Setup Parameters.

PARAMETER	SYMBOL	VALUE	UNITS
Rated power	P_N	16	kW
Rated voltage	V_N	400	V
Rated current	I_N	23.1	A
Rated frequency	f_N	50	Hz
DC link voltage	V_{dc}	730	V
Sampling time	T_s	62.5	μs
Grid resistance	R_{grid}	0.116	Ω
Grid inductance	L_{grid}	3	mH
Voltage @ steady state	V_0	400	$V_{LL,RMS}$
Frequency @ steady state	f_0	50	Hz
Active power ref. @ steady state in Fig. 10	P_{ref}	4	kW
Reactive power ref. @ steady state in Fig. 10	Q_{ref}	0	kVar
Active power ref. @ steady state in Fig. 9	P_{ref}	16	kW
Reactive power ref. @ steady state in Fig. 9	Q_{ref}	-5	kVar
Filter inductor	L	1000	μH
Filter capacitor	C	10	μF
Parallel filter resistor	R_C	1	MΩ
Frequency droop coefficient	m_ω	-3.1416	rad/Ws
Voltage droop coefficient	m_V	-16.33	V/Var
Bandwidth of power filter	ω_{LPF}	314.16	rad/s
Virtual capacitor	C	249.4	mF
Virtual inductor	L	40.63	μH
Voltage-scaling factor	k_v	230.94	V/V
Current-scaling factor	k_i	0.0433	A/A
Speed constant	ζ	16.11	$1/sV^2$
coupling angle	φ	1.57	rad
Proportional gain - current control	$k_{P,I}$	0.4234	Ω
Integral time const. - current control	$T_{i,I}$	–	s/Ω
Resonator bandwidth - current control	$\omega_{BW,I}$	–	rad/s
Resonator phase lead - current control	ϕ_I	0	rad
Proportional gain - DLVC	$k_{P,V,DL}$	0.1417	$1/\Omega$
Integral time const. - DLVC	$T_{i,V,SL}$	0.000514	Ωs
Resonator bandwidth - DLVC	$\omega_{BW,V}$	6.2832	rad/s
Resonator phase lead - DLVC	ϕ_V	0	rad
Proportional gain - SLVC	$k_{P,V,SL}$	0.06	V/V
Integral time const. - SLVC	$T_{i,V,SL}$	0.000514	s
Resonator bandwidth - SLVC	$\omega_{BW,V}$	6.2832	rad/s
Resonator phase lead - SLVC	ϕ_V	0	rad
Active damping factor - DLVC	K_{rc}	14.02	Ω
Active damping bandwidth - DLVC	ω_{rc}	52276	rad/s
Active damping factor - SLVC	K_{rc}	7.92	Ω
Active damping bandwidth - SLVC	ω_{rc}	33175	rad/s
Active damping factor - OLVC	K_{rc}	7.92	Ω
Active damping bandwidth - OLVC	ω_{rc}	33175	rad/s
PWM and sampling time delay	T_d	$3.5T_s$	s

b: INNER INVERTER OUTPUT CONTROL STATES

Contribution to own states:

$$\mathbf{A}_d = -\frac{1}{T_d}\mathbf{I} - \omega_0\mathbf{D}_-,\ \mathbf{A}_{ad} = -\omega_{rc}\mathbf{I} - \omega_0\mathbf{D}_-$$

$$\mathbf{A}_{ctrl} = \begin{bmatrix} -2\gamma_1\mathbf{I}_2 & -(\gamma_1^2+\gamma_2^2)\mathbf{I} & -\gamma_1\gamma_2^2\mathbf{I} & -\frac{1}{4}\gamma_1^2\gamma_2^2\mathbf{I} \\ \mathbf{I} & \mathbf{0}_2 & \mathbf{0}_2 & \mathbf{0}_2 \\ \mathbf{0}_2 & \mathbf{I} & \mathbf{0}_2 & \mathbf{0}_2 \\ \mathbf{0}_2 & \mathbf{0}_2 & \mathbf{I} & \mathbf{0}_2 \end{bmatrix}$$

Contribution to other states:

$$\mathbf{A}_{d/el} = \left[\frac{1}{L_f}\mathbf{I}\ \mathbf{0}_{2\times4}\right]^T,\ \mathbf{A}_{d/ad} = \frac{K_{rc}}{L_f}\mathbf{I},\ \mathbf{A}_{ad/d} = -\frac{1}{T_d}\mathbf{I}$$

$$\mathbf{A}_{ctrl/d} = \frac{k_{P,C}}{T_d}\left[\gamma_1\mathbf{I}\ \gamma_1^2\mathbf{I} - \frac{\gamma_1\gamma_2}{2}\mathbf{D}_-\ \frac{\gamma_1\gamma_2^2}{2}\mathbf{I}\ \frac{\gamma_1^2\gamma_2^2}{4}\mathbf{I}\right]$$

with $\gamma_1 = 2\omega_{BW}$, $\gamma_2 = 2\omega_0$, zero matrix $\mathbf{0}$ anti-diagonal matrix $\mathbf{D}_- = \text{adiag}(-1, 1)$ and identity matrix $\mathbf{I} = \text{diag}(1, 1)$

c: POWER-RELATED CONTROL STATES

Contribution to own states:

$$\mathbf{A}_{droop} = \begin{bmatrix} -\omega_{LPF}\mathbf{I} & \mathbf{0}_{2\times1} \\ \frac{m_\omega}{P_N}\mathbf{E} & 0 \end{bmatrix}$$

$$\mathbf{A}_{\mathrm{VOC}} = \mu_1\mathbf{I} + \mu_2\mathbf{D}_- + \begin{bmatrix} v_{\mathrm{C,d},0}(\mu_3 - \frac{2\zeta}{k_{\mathrm{v}}^2}v_{\mathrm{C,d},0}) & -v_{\mathrm{C,q},0}(\mu_3 - \frac{2\zeta}{k_{\mathrm{v}}^2}v_{\mathrm{C,d},0}) \\ -v_{\mathrm{C,d},0}(\mu_4 - \frac{2\zeta}{k_{\mathrm{v}}^2}v_{\mathrm{C,q},0}) & -v_{\mathrm{C,q},0}(\mu_4 - \frac{2\zeta}{k_{\mathrm{v}}^2}v_{\mathrm{C,q},0}) \end{bmatrix}$$

Contribution to other states:

$$\mathbf{A}_{\mathrm{droop/ctrl}} = \frac{k_{\mathrm{p,V}}}{T_{\mathrm{i,V}}}\begin{bmatrix} 0 & m_{\mathrm{V}}\cos\delta_0 & -|v_{\mathrm{C,dq},0}|\sin\delta_0 \\ 0 & m_{\mathrm{V}}\sin\delta_0 & |v_{\mathrm{C,dq},0}|\cos\delta_0 \\ \mathbf{0}_{6\times1} & \mathbf{0}_{6\times1} & \mathbf{0}_{6\times1} \end{bmatrix}$$

$$\mathbf{A}_{\mathrm{droop/d}} = \frac{k_{\mathrm{p,V}}k_{\mathrm{p,C}}}{T_{\mathrm{d}}}\begin{bmatrix} 0 & m_{\mathrm{V}}\cos\delta_0 & -|v_{\mathrm{C,dq},0}|\sin\delta_0 \\ 0 & m_{\mathrm{V}}\sin\delta_0 & |v_{\mathrm{C,dq},0}|\cos\delta_0 \end{bmatrix}$$

$$\mathbf{A}_{\mathrm{VOC/ctrl}} = \frac{k_{\mathrm{p,V}}}{T_{\mathrm{i,V}}}\begin{bmatrix} \mathbf{I} \\ \mathbf{0}_{6\times1} \end{bmatrix},\ \mathbf{A}_{\mathrm{VOC/d}} = \frac{k_{\mathrm{p,C}}k_{\mathrm{p,V}}}{T_{\mathrm{d}}}\mathbf{I}$$

with

$$\mu_1 = \frac{2k_{\mathrm{i}}k_{\mathrm{v}}Q_{\mathrm{set},0}}{3|v_{\mathrm{C,dq},0}|} + \frac{\zeta}{k_{\mathrm{v}}^2}(2V_{\mathrm{N}}^2 - |v_{\mathrm{C,dq},0}|^2),$$
$$\mu_2 = \frac{2k_{\mathrm{i}}k_{\mathrm{v}}P_{\mathrm{set},0}}{3|v_{\mathrm{C,dq},0}|}$$
$$\mu_3 = \frac{4(P_{\mathrm{set},0}v_{\mathrm{C,q},0} - Q_{\mathrm{set},0}v_{\mathrm{C,d},0})}{3C|v_{\mathrm{C,dq},0}|},$$
$$\mu_4 = \frac{4(P_{\mathrm{set},0}v_{\mathrm{C,d},0} + Q_{\mathrm{set},0}v_{\mathrm{C,q},0})}{3C|v_{\mathrm{C,dq},0}|}$$

zero matrix $\mathbf{0}$, identity matrix $\mathbf{I} = \mathrm{diag}(1, 1)$, vector $\mathbf{E} = \begin{bmatrix}1 & 0\end{bmatrix}$ and anti-diagonal matrix $\mathbf{D}_- = \mathrm{adiag}(-1, 1)$ The the steady state is defined by $i_{\mathrm{grid,dq},0}$, $v_{\mathrm{C,dq},0}$ and δ_0.

The complete linearised state-space model of the droop-controlled converter coupled with a passive grid is defined by the following $n = 21$ states

$$\mathbf{A} = \begin{bmatrix} \mathbf{A}_{\mathrm{el}} & \mathbf{0}_{6\times2} & \mathbf{0}_{6\times8} & \mathbf{0}_{6\times3} & \mathbf{A}_{\mathrm{d/el}} \\ \mathbf{A}_{\mathrm{el/ad}} & \mathbf{A}_{\mathrm{ad}} & \mathbf{0}_{2\times8} & \mathbf{0}_{2\times3} & \mathbf{A}_{\mathrm{d/ad}} \\ \mathbf{A}_{\mathrm{el/ctrl}} & \mathbf{0}_{8\times2} & \mathbf{A}_{\mathrm{ctrl}} & \mathbf{A}_{\mathrm{droop/ctrl}} & \mathbf{0}_{8\times2} \\ \mathbf{A}_{\mathrm{el/droop}} & \mathbf{0}_{3\times2} & \mathbf{0}_{3\times8} & \mathbf{A}_{\mathrm{droop}} & \mathbf{0}_{3\times2} \\ \mathbf{A}_{\mathrm{el/d}} & \mathbf{A}_{\mathrm{ad/d}} & \mathbf{A}_{\mathrm{ctrl/d}} & \mathbf{A}_{\mathrm{droop/d}} & \mathbf{A}_{\mathrm{d}} \end{bmatrix},$$
$$\mathbf{B} = \frac{1}{L_{\mathrm{grid}}}\begin{bmatrix}\mathbf{0}_{2\mathrm{x}4} & -\mathbf{I} & K_{\mathrm{rc}}\mathbf{I} & \mathbf{0}_{2\mathrm{x}13}\end{bmatrix}^{\mathrm{T}},$$
$$\mathbf{C} = \begin{bmatrix}\mathbf{0}_{2\times4} & \mathbf{I} & \mathbf{0}_{2\times15}\end{bmatrix},$$
$$\mathbf{D} = \begin{bmatrix}\mathbf{0}_{21\times1}\end{bmatrix},$$

with zero matrix $\mathbf{0}$ and identity matrix $\mathbf{I} = \mathrm{diag}(1, 1)$, along with the state vector in (63) and the input vector in (64).

The VOC-controlled converter is modelled based on the following $n = 20$ states

$$\mathbf{A} = \begin{bmatrix} \mathbf{A}_{\mathrm{el}} & \mathbf{0}_{6\times2} & \mathbf{0}_{6\times8} & \mathbf{0}_{6\times2} & \mathbf{A}_{\mathrm{d/el}} \\ \mathbf{A}_{\mathrm{el/ad}} & \mathbf{A}_{\mathrm{ad}} & \mathbf{0}_{2\times8} & \mathbf{0}_{2\times2} & \mathbf{A}_{\mathrm{d/ad}} \\ \mathbf{A}_{\mathrm{el/ctrl}} & \mathbf{0}_{8\times2} & \mathbf{A}_{\mathrm{ctrl}} & \mathbf{A}_{\mathrm{VOC/ctrl}} & \mathbf{0}_{8\times2} \\ \mathbf{A}_{\mathrm{el/VOC}} & \mathbf{0}_{2\times2} & \mathbf{0}_{2\times8} & \mathbf{A}_{\mathrm{VOC}} & \mathbf{0}_{2\times2} \\ \mathbf{A}_{\mathrm{el/d}} & \mathbf{A}_{\mathrm{ad/d}} & \mathbf{A}_{\mathrm{ctrl/d}} & \mathbf{A}_{\mathrm{VOC/d}} & \mathbf{A}_{\mathrm{d}} \end{bmatrix},$$
$$\mathbf{B} = \frac{1}{L_{\mathrm{grid}}}\begin{bmatrix}\mathbf{0}_{2\mathrm{x}4} & -\mathbf{I} & K_{\mathrm{rc}}\mathbf{I} & \mathbf{0}_{2\mathrm{x}12}\end{bmatrix}^{\mathrm{T}},$$
$$\mathbf{C} = \begin{bmatrix}\mathbf{0}_{2\times4} & \mathbf{I} & \mathbf{0}_{2\times14}\end{bmatrix},$$
$$\mathbf{D} = \begin{bmatrix}\mathbf{0}_{20\times1}\end{bmatrix},$$

with zero matrix $\mathbf{0}$ and identity matrix $\mathbf{I} = \mathrm{diag}(1, 1)$, in combination with the state vector in (62) and the input vector in (64).

$$\mathbf{A} = \begin{bmatrix} 1 - \frac{3}{4}\overline{\boldsymbol{i_0}}\frac{\omega_{\mathrm{LP}}}{s+\omega_{\mathrm{LP}}-j\omega_0}G_{\mathrm{cl}}(s)j(\hat{V}_0\frac{m_\omega}{P_{\mathrm{N}}(s-j\omega_0)} - \frac{m_{\mathrm{V}}}{P_{\mathrm{N}}}) & -\frac{3}{4}\boldsymbol{i_0}\frac{\omega_{\mathrm{LP}}}{s+\omega_{\mathrm{LP}}-j\omega_0}G_{\mathrm{cl}}(s)j(\hat{V}_0\frac{m_\omega}{P_{\mathrm{N}}(s-j\omega_0)} + \frac{m_{\mathrm{V}}}{P_{\mathrm{N}}}) \\ -\frac{3}{4}\boldsymbol{i_0}\frac{\omega_{\mathrm{LP}}}{j\omega_{\mathrm{N}}-s+\omega_{\mathrm{LP}}}G_{\mathrm{cl}}(2j\omega_0-s)j(\hat{V}_0\frac{m_\omega}{P_{\mathrm{N}}(j\omega_0-s)} + \frac{m_{\mathrm{V}}}{P_{\mathrm{N}}}) & 1 - \frac{3}{4}\overline{\boldsymbol{i_0}}\frac{\omega_{\mathrm{LP}}}{j\omega_0-s+\omega_{\mathrm{LP}}}G_{\mathrm{cl}}(2j\omega_0-s)j(\hat{V}_0\frac{m_\omega}{P_{\mathrm{N}}(j\omega_0-s)} - \frac{m_{\mathrm{V}}}{P_{\mathrm{N}}}) \end{bmatrix},$$
$$\underline{B} = \begin{bmatrix} -Z_{\mathrm{C}}(s) + j\frac{3}{4}\hat{V}_0G_{\mathrm{cl}}(s)\frac{\omega_{\mathrm{LP}}}{s-j\omega_0+\omega_{\mathrm{LP}}}(\hat{V}_0\frac{m_\omega}{P_{\mathrm{N}}(s-j\omega_0)} + \frac{m_{\mathrm{V}}}{P_{\mathrm{N}}}) \\ j\frac{3}{4}\hat{V}_0G_{\mathrm{cl}}(2j\omega_0-s)\frac{\omega_{\mathrm{LP}}}{j\omega_0-s+\omega_{\mathrm{LP}}}(\hat{V}_0\frac{m_\omega}{P_{\mathrm{N}}(j\omega_0-s)} - \frac{m_{\mathrm{V}}}{P_{\mathrm{N}}}) \end{bmatrix}\boldsymbol{di}(s),$$
$$\underline{x} = \begin{bmatrix}\boldsymbol{dV}(s) \\ \boldsymbol{dV}(2j\omega_0-s)\end{bmatrix} \rightarrow \mathbf{A}\underline{x} = \begin{bmatrix}A_{1,1} & A_{1,2} \\ A_{2,1} & A_{2,2}\end{bmatrix}\begin{bmatrix}x_1 \\ x_2\end{bmatrix} = \underline{B},$$

$$\mathbf{A} = \begin{bmatrix} 3CV_0^2e^{-j\varphi}\left(k_{\mathrm{v}}^2(s-j\omega_{\mathrm{N}}) - 2\zeta(V_{\mathrm{N}}^2 - V_0^2)\right) - 2k_{\mathrm{i}}k_{\mathrm{v}}^3\overline{\mathbf{S}_{\mathbf{ref}}} - 3C\zeta V_0^4e^{-j\varphi} \\ -3C\zeta V_0^4e^{-j\varphi}3CV_0^2e^{-j\varphi}\left(k_{\mathrm{v}}^2(2j\omega_0 - s - j\omega_{\mathrm{N}}) - 2\zeta(V_{\mathrm{N}}^2 - V_0^2)\right) - 2k_{\mathrm{i}}k_{\mathrm{v}}^3\overline{\mathbf{S}_{\mathbf{ref}}} \end{bmatrix},$$
$$\underline{B} = \begin{bmatrix}3V_0^2k_{\mathrm{i}}k_{\mathrm{v}}^3 \\ 0\end{bmatrix}\boldsymbol{di}(s),$$
$$\underline{x} = \begin{bmatrix}\boldsymbol{dV}(s) \\ \boldsymbol{dV}(2j\omega_0 - s)\end{bmatrix} \rightarrow \mathbf{A} \otimes \underline{x} = \begin{bmatrix}A_{1,1}x_1 + A_{1,2}\overline{x}_2 \\ A_{2,1}\overline{x}_1 + A_{2,2}x_2\end{bmatrix} = \underline{B},$$

APPENDIX C
PHASE-PORTRAIT MODELS

The conventional phase-portrait model of a VOC-controlled converter can be derived based on (6) - (7) with the derivatives of the voltage magnitude $\dot{V}(t) = \frac{\mathrm{d}}{\mathrm{d}t}\frac{\sqrt{v_{\mathrm{ref},\alpha}(t)^2+v_{\mathrm{ref},\beta}(t)^2}}{\sqrt{2}}$ and its phase angle $\dot{\delta}(t) = \frac{\mathrm{d}}{\mathrm{d}t}\arctan\frac{v_{\mathrm{ref},\beta}(t)}{v_{\mathrm{ref},\alpha(\mathrm{t})}}$

$$\dot{V}(t) = \frac{\zeta}{k_{\mathrm{v}}^2}V(t)\left(2V_{\mathrm{N}}^2 - V(t)^2\right) + \frac{k_{\mathrm{v}}k_{\mathrm{i}}}{C}\left(\frac{2}{3V(t)}\mathrm{Re}\{e^{-j\varphi}S_{\mathrm{ref}}(t)\}\right.$$
$$\left. + \mathrm{Re}\left\{\frac{Z_{\mathrm{grid}}}{|Z_{\mathrm{grid}}|^2}\left(E(t)e^{j(\delta(t)-\varphi)} - V(t)e^{-j\varphi}\right)\right\}\right),$$
$$\dot{\delta}(t) = \omega_{\mathrm{N}} - \frac{k_{\mathrm{v}}k_{\mathrm{i}}}{C}\left(\frac{2}{3V(t)^2}\mathrm{Im}\{e^{-j\varphi}S_{\mathrm{ref}}(t)\}\right.$$
$$\left. + \mathrm{Im}\left\{\frac{Z_{\mathrm{grid}}}{|Z_{\mathrm{grid}}|^2}\left(\frac{E(t)}{V(t)}e^{j(\varphi-\delta(t))} - V(t)e^{-j\varphi}\right)\right\}\right).$$

APPENDIX D
SETUP PARAMETERS

The active damping scheme has been designed iteratively in order to achieve a good damping performance of the filter resonance while passive damping is negligible. The proportional gain of the inner current control loop is limited by the minimal gain margin $\mathrm{GM} = \frac{1}{\sqrt{2}}$ for the LC resonance peak of the equivalent transfer function. The outer voltage control loop is designed based on the concept in [51], adapted for the equivalent transfer function and applied for the phase margin $\mathrm{PM} = 55°$. This procedure and the concept in [37] are utilised to design the single loop voltage control for $\mathrm{PM} = 55°$.

All parameters of the considered study case are listed in Table 2.

REFERENCES

[1] J. Rocabert, A. Luna, F. Blaabjerg, and P. Rodríguez, "Control of power converters in AC microgrids," *IEEE Trans. Power Electron.*, vol. 27, no. 11, pp. 4734–4749, Nov. 2012.

[2] M. Farrokhabadi *et al.*, "Microgrid stability definitions, analysis, and examples," *IEEE Trans. Power Syst.*, vol. 35, no. 1, pp. 13–29, Jan. 2020.

[3] R. Rosso, M. Andresen, S. Engelken, and M. Liserre, "Analysis of the interaction among power converters through their synchronization mechanism," *IEEE Trans. Power Electron.*, vol. 34, no. 12, pp. 12321–12332, Dec. 2019.

[4] X. Wang, M. G. Taul, H. Wu, Y. Liao, F. Blaabjerg, and L. Harnefors, "Grid-synchronization stability of converter-based resources—An overview," *IEEE Open J. Ind. Appl.*, vol. 1, pp. 115–134, 2020.

[5] R. Rosso, S. Engelken, and M. Liserre, "Analysis of the parallel operation between synchronverters and PLL-based converters," in *Proc. IEEE Energy Convers. Congr. Expo. (ECCE)*, Sep. 2019, pp. 2583–2590.

[6] J. Chen, M. Liu, F. Milano, and T. O'Donnell, "100% converter-interfaced generation using virtual synchronous generator control: A case study based on the irish system," *Electr. Power Syst. Res.*, vol. 187, Oct. 2020, Art. no. 106475.

[7] D. Ramasubramanian, Z. Yu, R. Ayyanar, V. Vittal, and J. Undrill, "Converter model for representing converter interfaced generation in large scale grid simulations," *IEEE Trans. Power Syst.*, vol. 32, no. 1, pp. 765–773, Jan. 2017.

[8] P. Kundur, N. Balu, and M. Lauby, *Power System Stability and Control* (EPRI Power System Engineering Series). New York, NY, USA: McGraw-Hill, 1994.

[9] N. Pogaku, M. Prodanovic, and T. C. Green, "Modeling, analysis and testing of autonomous operation of an inverter-based microgrid," *IEEE Trans. Power Electron.*, vol. 22, no. 2, pp. 613–625, Mar. 2007.

[10] Y. Han, M. Yang, P. Yang, L. Xu, X. Fang, K. Zhang, and F. Blaabjerg, "Reduced-order model for dynamic stability analysis of single-phase islanded microgrid with BPF-based droop control scheme," *IEEE Access*, vol. 7, pp. 157859–157872, 2019.

[11] C. L. DeMarco and J. Wassner, "A generalized eigenvalue perturbation approach to coherency," in *Proc. Int. Conf. Control Appl.*, 1995, pp. 611–617.

[12] P. J. Hart, R. H. Lasseter, and T. M. Jahns, "Coherency identification and aggregation in grid-forming droop-controlled inverter networks," *IEEE Trans. Ind. Appl.*, vol. 55, no. 3, pp. 2219–2231, May 2019.

[13] L. P. Kunjumuhammed, B. C. Pal, C. Oates, and K. J. Dyke, "The adequacy of the present practice in dynamic aggregated modeling of wind farm systems," *IEEE Trans. Sustain. Energy*, vol. 8, no. 1, pp. 23–32, Jan. 2017.

[14] Y. Gu, N. Bottrell, and T. C. Green, "Reduced-order models for representing converters in power system studies," *IEEE Trans. Power Electron.*, vol. 33, no. 4, pp. 3644–3654, Apr. 2018.

[15] B. Shakerighadi, E. Ebrahimzadeh, F. Blaabjerg, and C. L. Bak, "Lyapunov- and eigenvalue-based stability assessment of the grid-connected voltage source converter," in *Proc. IEEE Int. Power Electron. Appl. Conf. Expo. (PEAC)*, Nov. 2018.

[16] M. Kabalan, P. Singh, and D. Niebur, "Large signal Lyapunov-based stability studies in microgrids: A review," *IEEE Trans. Smart Grid*, vol. 8, no. 5, pp. 2287–2295, Sep. 2017.

[17] D. Pan, X. Wang, F. Liu, and R. Shi, "Transient stability of voltage-source converters with grid-forming control: A design-oriented study," *IEEE J. Emerg. Sel. Topics Power Electron.*, vol. 8, no. 2, pp. 1019–1033, Jun. 2020.

[18] M. Rasheduzzaman, J. A. Mueller, and J. W. Kimball, "An accurate small-signal model of Inverter- dominated islanded microgrids using *dq* reference frame," *IEEE J. Emerg. Sel. Topics Power Electron.*, vol. 2, no. 4, pp. 1070–1080, Dec. 2014.

[19] M. Amin and M. Molinas, "Small-signal stability assessment of power electronics based power systems: A discussion of impedance- and eigenvalue-based methods," *IEEE Trans. Ind. Appl.*, vol. 53, no. 5, pp. 5014–5030, Sep. 2017.

[20] L. Harnefors, M. Bongiorno, and S. Lundberg, "Input-admittance calculation and shaping for controlled voltage-source converters," *IEEE Trans. Ind. Electron.*, vol. 54, no. 6, pp. 3323–3334, Dec. 2007.

[21] X. Wang, F. Blaabjerg, and W. Wu, "Modeling and analysis of harmonic stability in an AC power-electronics-based power system," *IEEE Trans. Power Electron.*, vol. 29, no. 12, pp. 6421–6432, Dec. 2014.

[22] M. Sarstedt, M. Dokus, J. Gerster, N. Himker, L. Hofmann, S. Lehnhoff, and A. Mertens, "Standardized evaluation of multi-level grid control strategies for future converter-dominated electric energy systems," *at-Automatisierungstechnik*, vol. 67, no. 11, pp. 936–957, Nov. 2019.

[23] M. Dokus and A. Mertens, "On the stability of converter-dominated power systems: Impedance-based analysis," in *Proc. Int. Conf. Smart Grids Energy Syst.*, 2020.

[24] C. Zhang, X. Cai, Z. Li, A. Rygg, and M. Molinas, "Properties and physical interpretation of the dynamic interactions between voltage source converters and grid: Electrical oscillation and its stability control," *IET Power Electron.*, vol. 10, no. 8, pp. 894–902, Jun. 2017.

[25] M. G. Taul, X. Wang, P. Davari, and F. Blaabjerg, "Reduced-order and aggregated modeling of large-signal synchronization stability for multi-converter systems," *IEEE J. Emerg. Sel. Topics Power Electron.*, early access, Aug. 10, 2021, doi: 10.1109/JESTPE.2020.3015293.

[26] M. G. Taul, S. Golestan, X. Wang, P. Davari, and F. Blaabjerg, "Modeling of converter synchronization stability under grid faults: The general case," *IEEE J. Emerg. Sel. Topics Power Electron.*, early access, Sep. 21, 2020, doi: 10.1109/JESTPE.2020.3024940.

[27] X. Guo, Z. Lu, B. Wang, X. Sun, L. Wang, and J. M. Guerrero, "Dynamic phasors-based modeling and stability analysis of droop-controlled inverters for microgrid applications," *IEEE Trans. Smart Grid*, vol. 5, no. 6, pp. 2980–2987, Nov. 2014.

[28] H. Yu, J. Su, H. Wang, Y. Wang, and Y. Shi, "Modelling method and applicability analysis of a reduced-order inverter model for microgrid applications," *IET Power Electron.*, vol. 13, no. 12, pp. 2638–2650, Sep. 2020.

[29] R. H. Lasseter, "MicroGrids," in *Proc. IEEE Power Eng. Soc. Winter Meeting*, vol. 1, Jan. 2002, pp. 305–308.

[30] M. C. Chandorkar, D. M. Divan, and R. Adapa, "Control of parallel connected inverters in standalone AC supply systems," *IEEE Trans. Ind. Appl.*, vol. 29, no. 1, pp. 136–143, Jan. 1993.

[31] M. Dokus, F. Stallmann, and A. Mertens, "Sequence impedance-based stability analysis of AC microgrids controlled by virtual synchronous generator control methods," in *Proc. 21st IFAC World Congr. Autom. Control*, 2020.
[32] J. Chen and T. O'Donnell, "Analysis of virtual synchronous generator control and its response based on transfer functions," *IET Power Electron.*, vol. 12, no. 11, pp. 2965–2977, Sep. 2019.
[33] M. Lu, S. Dutta, V. Purba, S. Dhople, and B. Johnson, "A grid-compatible virtual oscillator controller: Analysis and design," in *Proc. IEEE Energy Convers. Congr. Expo. (ECCE)*, Sep. 2019, pp. 2643–2649.
[34] M. Sinha, F. Dorfler, B. B. Johnson, and S. V. Dhople, "Uncovering droop control laws embedded within the nonlinear dynamics of van der pol oscillators," *IEEE Trans. Control Netw. Syst.*, vol. 4, no. 2, pp. 347–358, Jun. 2017.
[35] Z. Shi, J. Li, H. I. Nurdin, and J. E. Fletcher, "Comparison of virtual oscillator and droop controlled islanded three-phase microgrids," *IEEE Trans. Energy Convers.*, vol. 34, no. 4, pp. 1769–1780, Dec. 2019.
[36] X. Wang, F. Blaabjerg, and P. C. Loh, "Virtual RC damping of LCL-filtered voltage source converters with extended selective harmonic compensation," *IEEE Trans. Power Electron.*, vol. 30, no. 9, pp. 4726–4737, Sep. 2015.
[37] X. Wang, P. C. Loh, and F. Blaabjerg, "Stability analysis and controller synthesis for single-loop voltage-controlled VSIs," *IEEE Trans. Power Electron.*, vol. 32, no. 9, pp. 7394–7404, Sep. 2017.
[38] R. Rosso, S. Engelken, and M. Liserre, "Robust stability analysis of synchronverters operating in parallel," *IEEE Trans. Power Electron.*, vol. 34, no. 11, pp. 11309–11319, Nov. 2019.
[39] L. Harnefors, R. Finger, X. Wang, H. Bai, and F. Blaabjerg, "VSC input-admittance modeling and analysis above the nyquist frequency for passivity-based stability assessment," *IEEE Trans. Ind. Electron.*, vol. 64, no. 8, pp. 6362–6370, Aug. 2017.
[40] M. Dokus and A. Mertens, "Sequence impedance-based stability analysis of droop-controlled AC microgrids," in *Proc. IEEE 10th Int. Symp. Power Electron. Distrib. Gener. Syst. (PEDG)*, Jun. 2019, pp. 768–773.
[41] A. Rygg, M. Molinas, C. Zhang, and X. Cai, "On the equivalence and impact on stability of impedance modeling of power electronic converters in different domains," *IEEE J. Emerg. Sel. Topics Power Electron.*, vol. 5, no. 4, pp. 1444–1454, Dec. 2017.
[42] I. Vieto and J. Sun, "Sequence impedance modeling and converter-grid resonance analysis considering DC bus dynamics and mirrored harmonics," in *Proc. IEEE 19th Workshop Control Modeling Power Electron. (COMPEL)*, Jun. 2018, pp. 1–8.
[43] H. Zhang, X. Wang, L. Harnefors, H. Gong, J.-P. Hasler, and H.-P. Nee, "SISO transfer functions for stability analysis of grid-connected voltage-source converters," *IEEE Trans. Ind. Appl.*, vol. 55, no. 3, pp. 2931–2941, May 2019.
[44] L. Harnefors, "Modeling of three-phase dynamic systems using complex transfer functions and transfer matrices," *IEEE Trans. Ind. Electron.*, vol. 54, no. 4, pp. 2239–2248, Aug. 2007.
[45] K. Yu, Q. Ai, S. Wang, J. Ni, and T. Lv, "Analysis and optimization of droop controller for microgrid system based on small-signal dynamic model," *IEEE Trans. Smart Grid*, vol. 7, no. 2, pp. 695–705, Mar. 2016.
[46] T. Demiray, "Simulation of power system dynamics using dynamic phasor models," Ph.D. dissertation, ETH Zurich, Zürich, Switzerland, 2008.
[47] P. J. Hart, J. Goldman, R. H. Lasseter, and T. M. Jahns, "Impact of harmonics and unbalance on the dynamics of grid-forming, frequency-droop-controlled inverters," *IEEE J. Emerg. Sel. Topics Power Electron.*, vol. 8, no. 2, pp. 976–990, Jun. 2020.
[48] M. Dokus and A. Mertens, "Sequence impedance characteristics of grid-forming converter controls," in *Proc. IEEE 11th Int. Symp. Power Electron. Distrib. Gener. Syst. (PEDG)*, Sep. 2020, pp. 413–420.
[49] J. Chen and T. O'Donnell, "Parameter constraints for virtual synchronous generator considering stability," *IEEE Trans. Power Syst.*, vol. 34, no. 3, pp. 2479–2481, May 2019.
[50] F. Stallmann and A. Mertens, "Sequence impedance modeling of the matching control and comparison with virtual synchronous generator," in *Proc. IEEE 11th Int. Symp. Power Electron. Distrib. Gener. Syst. (PEDG)*, Sep. 2020, pp. 421–428.
[51] D. G. Holmes, T. A. Lipo, B. P. McGrath, and W. Y. Kong, "Optimized design of stationary frame three phase AC current regulators," *IEEE Trans. Power Electron.*, vol. 24, no. 11, pp. 2417–2426, Nov. 2009.

MARC DOKUS (Student Member, IEEE) received the B.Eng. degree in renewable energy technology from the Flensburg University of Applied Sciences, Flensburg, Germany, in 2013, and the M.Sc. degree in electrical engineering from Leibniz University Hannover, Germany, in 2016. He is currently pursuing the Ph.D. degree in electrical engineering from the Institute for Drive Systems and Power Electronics, Leibniz University Hannover.

From 2013 to 2014, he was with Moeller Operating Engineering GmbH, Itzehoe, Germany, where he was responsible for the grid integration and certification of several distributed power plants and units. In 2016, he was a Visiting Scholar with the University of Wisconsin–Madison. His current research interests include the stability analysis and control of grid-connected converter system in power networks.

AXEL MERTENS (Senior Member, IEEE) received the Dipl.-Ing. and Dr.-Ing. (Ph.D.) degrees from RWTH Aachen, Germany, in 1987 and 1992, respectively.

In 1989, he was a Visiting Scholar with the University of Wisconsin at Madison. From 1993 to 2004, he was with Siemens AG, Erlangen and Nürnberg, Germany, with responsibilities for the control of large drives including a variety of converter topologies, and for a product range of medium voltage inverters. In 2004, he was a Professor of power electronics and drives with Leibniz University Hannover, Germany. He served as the Department Chair for the Department of Electrical Engineering and Computer Science and also a Spokesman for the Energy Research Center LiFE 2050, Leibniz University Hannover. In addition to his academic duties, he had responsibilities within Fraunhofer IFAM, Bremen, and within Fraunhofer IEE, Kassel. He has published more than 180 conference and journal articles. His research interests include the application of WBG devices in e-mobility, self-sensing control of electric machines, the monitoring of high-power electronic devices, control of modular multilevel converters, and control of converters in grids.

Prof. Mertens has been a member of the PELS AdCom since 2019. He served as the Chairman for the IEEE Joint IAS/PELS/IES German Chapter. He is an Associate Editor of the IEEE TRANSACTIONS ON POWER ELECTRONICS.